Langmuir Turbulence in the Arctic Ocean: Insights From a Coupled Sea Ice –Wave Model

Aikaterini Tavri[1], Chris Horvat[1], Brodie Pearson[2], Guillaume Boutin[3], Anne Hansen[2], and Ara Lee[2]

[1]Brown University, Providence, RI, USA
[2]Oregon State University, Corvallis, OR, USA
[3]Nansen Environmental and Remote Sensing Center and Bjerknes Centre for Climate Research, Bergen, Norway

Correspondence: Aikaterini Tavri aikaterini_tavri@brown.edu

Abstract. ~~Upper ocean mixing governs~~ Upper-ocean mixing regulates the vertical transport of heat, momentum, and tracers in the ocean surface boundary layer~~(OSBL), yet large-scale climate models often misrepresent its underlying processes, leading to significant uncertainty in sea ice and ocean predictions~~, yet its representation under sea ice remains highly uncertain. Langmuir turbulence (LT)~~is one of the primary mechanisms of mixing in the open ocean and is~~ , generated by the interaction of wind stress and wave-induced Stokes drift~~. Observations have confirmed LT activity~~ , is a dominant open-ocean mixing mechanism and has been observed in leads, polynyas, and the marginal ice zone (MIZ), ~~however its spatial and seasonal variability remains~~ but its Arctic-wide occurrence and modulation by sea ice and waves are poorly constrained. ~~In this study, we conduct the first Arctic-wide~~ Here we present the first pan-Arctic assessment of LT potential using a ~~coupled sea ice–wave model that integrates neXtSIM and WAVEWATCH III. We analyze the spatiotemporal variability of LT by examining model-resolved turbulent~~ fully coupled sea ice–wave modeling framework integrating *neXtSIM* and *WAVEWATCH III*. Combining wind–wave forcing metrics with mixed-layer–integrated dissipation and vertical kinetic energy ~~within the OSBL. Our analysis reveals that LT potential is higher in the MIZ during~~ diagnostics, we show that LT-relevant forcing beneath sea ice is spatially confined and strongly intermittent. Conditions capable of sustaining LT occur primarily within the seasonal MIZ and arise episodically during late melt and freeze-up, ~~when partial sea ice cover allows intermittent wave propagation. Under these conditions, LT commonly coexists with wind-driven shear, forming a mixed-forcing regime that shapes upper-ocean energetics in response to evolving sea ice and wave states~~rather than as a persistent background state. Sea ice concentration ~~and wind–wave alignment strongly influence the intensity and distribution of LT-driven mixing . On average, LT contributes roughly 15% of the total upper-ocean dissipation~~ regulates the mean balance between wave- and shear-driven turbulence, while ice mechanical state, wave properties, and wind–wave misalignment control the efficiency of Langmuir-driven vertical motions without altering the underlying mixing regimes. As a result, LT in the Arctic MIZ ~~, with episodic wave-driven events during transitional ice periods doubling local mixing rates compared to wind-only conditions. This analysis highlights the energetic role of wave-induced mixing in the upper ocean, with potential implications for vertical momentum transport, mixed layer structure, and sea ice–ocean interactions in the Arctic.~~

most often coexists with wind-driven shear in mixed-forcing regimes, highlighting the need for regime-aware representations of upper-ocean mixing in climate models.

1 Introduction

The Arctic Ocean has traditionally been considered a region of weak upper-ocean mixing, primarily due to extensive sea ice cover that insulates the ocean from atmospheric forcing and dissipates wave energy (Morison et al., 1985; Pinkel, 2005). Under these conditions, turbulent exchange in the ocean surface boundary layer (OSBL) remains strongly suppressed, and vertical mixing occurs only during sporadic shear-driven and convective events. In recent decades, the rapid decline in sea ice, marked by the loss of multiyear ice, earlier seasonal melt onset, and expansion of open water area, has increasingly exposed the Arctic Ocean to wind and wave forcing, fundamentally shifting the traditional view (Stopa et al., 2016; Armitage et al., 2017; Muilwijk et al., 2024). These changes have amplified air–sea momentum transfer (Rainville et al., 2011; Dosser and Rainville, 2016) and expanded the Marginal Ice Zone (MIZ), a transitional region characterized by discontinuous ice cover that enables surface wave propagation and interaction with the floe field (Collins et al., 2018; Boutin et al., 2020).

Within the MIZ, surface gravity waves play a central role in mediating air–sea interaction. They modulate sea ice breakup and accelerate melt through enhanced mechanical stress and turbulent mixing (Thomson and Rogers, 2014; Thomson, 2022). Beyond direct wave breaking, surface waves also generate upper-ocean turbulence through Langmuir turbulence (LT), that develops when wind-forced shear aligns with wave-induced Stokes drift (Craik and Leibovich, 1976; Leibovich, 1983; McWilliams et al., 1997). LT forms coherent, counter-rotating Langmuir cells that vertically redistribute heat, momentum, and tracers, ~~(Skyllingstad and Denbo, 1995; D'Asaro, 2014; Kukulka et al., 2013; Gargett and Grosch, 2014)~~(Skyllingstad and Denbo, 1995; Kukulka , and it has emerged as a key regulator of mixed layer dynamics in the open ocean (Belcher et al., 2012; Yang et al., 2014). The absence of LT parameterizations in ocean general circulation models contributes to systematic biases in mixed layer depth and sea surface temperature, particularly in wind- and wave-active regions such as the Southern Ocean (Belcher et al., 2012; Li et al., 2019).

Large eddy simulation (LES) studies show that LT deepens the mixed layer and enhances vertical entrainment fluxes by up to an order of magnitude compared to shear-driven turbulence alone, while also moderately increasing momentum fluxes (McWilliams et al., 1997; Sullivan et al., 2007). Enhanced vertical mixing leads to elevated turbulent kinetic energy (TKE) and stronger entrainment across density interfaces (Polton and Belcher, 2007; Pearson et al., 2015; Ali et al., 2019). These insights have motivated the development of new LT parameterizations for large-scale models that incorporate wave–current interactions and Stokes production terms (Van Roekel et al., 2012; Harcourt, 2015; Li and Fox-Kemper, 2017). Despite these advances, existing parameterizations have not been systematically evaluated in sea ice-covered regions, where the physical environment deviates substantially from typical open-ocean conditions due to the sea ice dynamics (McWilliams and Sullivan, 2000; Smyth et al., 2002; Brenner and Horvat, 2024).

In the Arctic, sea ice modifies upper ocean mixing dynamics in several ways. It limits wave fetch, alters the directional spread of wave energy, and attenuates short-wavelength wave components - all of which reduce the magnitude and vertical extent of Stokes drift (Ardhuin et al., 2016, 2020; Li and Fox-Kemper, 2017). Meanwhile, ice motion and floe interactions introduce additional sources of surface shear and turbulence (Skyllingstad and Denbo, 2001). Observations show that waves propagate long distances under sea ice and significantly influence mixing near leads, polynyas, and the ice edge (Drucker et al., 2003;

Kirillov et al., 2013; Horvat et al., 2020; Cooper et al., 2022). The presence of Langmuir cells in sea ice openings, confirms that the LT mechanism remains active in ice-covered waters, albeit with intermittent occurrence and modified structure (Dethleff and Kempema, 2007; Voermans et al., 2019). Although prior studies on wave - ice interactions have primarily focused on mechanical breakup of sea ice (Collins et al., 2018; Squire, 2018), the turbulent mixing contributions of LT in sea ice covered regions remain largely unexplored. Recent modeling studies have incorporated wave - ice interactions to investigate localized upper-ocean mixing (Horvat et al., 2016; Manucharyan and Thompson, 2017; Cooper et al., 2022; Brenner and Horvat, 2024; Lo Piccolo et al., 2024), but no study has yet conducted a basin-wide, systematic evaluation of LT mixing potential under realistic Arctic sea ice and wave conditions.

In this study, we use a coupled sea ice - wave model that combines the neXtSIM Lagrangian sea ice model (Rampal et al., 2016) with the ~~WaveWatch~~ WAVEWATCH III (WW3) spectral wave model (Tolman et al., 2009). This modeling framework resolves surface Stokes drift, wave energy, and wind stress under evolving sea ice conditions. Using this information, we conduct an Arctic-wide assessment of LT potential under realistic wave - ~~ice interactions.~~ sea ice interaction. *LT potential* is defined as the amplitude of Langmuir forcing inferred from surface shear (friction velocity, u_*) and surface wave-induced Stokes drift ($u_{s(0)}$), independent of oceanic dynamical adjustment. Our primary objective is to identify when and where LT ~~mixing - supporting~~ mixing-supporting conditions emerge and persist, particularly in relation to seasonal sea ice advance and retreat. To ~~capture the influence of wind- wave directional alignment~~quantify the role of wind–wave coupling, we compute both the standard (turbulent) Langmuir number La_t and the projected Langmuir number La_{proj}, ~~which incorporates the cosine of the wind - Stokes drift angle to account for directional misalignment~~incorporating the orientation angle α_{LOW} of Van Roekel et al. (2012), which represents the empirically derived rotation of Langmuir cells toward the combined Eulerian and Stokes contributions. Using these metrics, we map surface turbulent mixing regimes across space and time and estimate the seasonal evolution of TKE dissipation and vertical kinetic energy (VKE) associated with LT ~~throughout~~ in the Arctic.

Section 2 ~~describes~~ details the coupled model configuration~~and details the computation~~ , the formulation of LT-relevant parameters, and an evaluation of the model inputs underpinning the LT metrics. Section 3 ~~presents our results, beginning with the spatiotemporal variability of~~ beginning with an assessment of LT-relevant wind and wave forcing in sea ice. We then map the ~~prevalence of distinct turbulent~~ spatial and temporal organization of upper-ocean mixing regimes and ~~quantify~~ their variability across the Arctic, before examining seasonal and regional patterns in ~~dissipation and~~ turbulent dissipation and normalized VKE. Finally, we assess the influence of wind - wave misalignment on LT energetics, highlighting where projected Langmuir diagnostics diverge from canonical estimates. Section 4 discusses the implications of our findings for Arctic mixed layer dynamics and model development and outlines key limitations of the study.

1.1 The ~~neXtSIM-WaveWatch~~ neXtSIM- WAVEWATCH III ~~Coupled Model~~

2 ~~Model Configuration~~

~~We employ a fully coupled~~ coupled model We use a coupled sea ice - wave ~~- sea ice~~ modeling framework that integrates the ~~spectral wave model WAVEWATCH III (WW3) with the~~ Lagrangian neXt-generation Sea Ice Model (neXtSIM) with the

WAVEWATCH III (WW3) spectral wave model using the OASIS-MCT coupler (Boutin et al., 2021). ~~WW3 simulates wave attenuation due to sea ice using parameterizations for scattering, inelastic flexure, and under-ice friction. These processes respond dynamically to changes in sea ice~~ NeXtSIM provides the evolving sea ice concentration, thickness, and ~~floe size distribution (Boutin et al., 2021). Sea ice morphology actively modulates Stokes drift profiles in WW3 by governing~~ floe-size distribution (FSD) that govern wave attenuation and ~~reshaping the directional structure of the wave field (Squire, 2018). The neXtSIM model captures sea icethermodynamics and dynamics. For this study, a key feature is its prognostic floe size distribution, which provides floe size information to~~ the directional filtering of wave energy. Unlike Eulerian models, neXtSIM employs a moving triangular mesh, undergoing periodic local remeshing to retain a nominal resolution equivalent to the 25 km stereographic grid used by WW3~~and influences wave attenuation alongside sea ice concentration and thickness. Previous studies have evaluated this coupling in idealized and realistic settings (Boutin et al., 2018; Ardhuin et al., 2018), showing that the wave-affected area matches~~ . Although the two components do not share the same mesh, fields are exchanged every 30 minutes via interpolation onto the WW3 exchange grid. NeXtSIM receives atmospheric forcing from the European Centre for Medium-Range Weather Forecasts (ECMWF) fifth generation reanalysis (ERA5) and oceanic forcing from the Global Ocean Physics GLORYS12V1 reanalysis, but it does not employ lateral boundary conditions for sea ice. Ice drifts freely across the open boundaries, with inflow treated as if external ice properties match those adjacent to the boundary (Ólason et al., 2025).

WW3 simulates wave propagation and attenuation in sea ice using the IS2+IC2 attenuation scheme, which combines scattering, inelastic flexure, and under-ice friction (Boutin et al., 2018). The southern boundary of the regional WW3 domain is set at 54°N, and lateral wave spectra are prescribed along this open boundary using the Ifremer global WW3 Modélisation et Analyse pour le Recherche Côtière (MARC) hindcast. WW3 is forced with the same hourly ERA5 winds used to force neXtSIM, but as in standard WW3 configurations, no ocean currents are applied, neglecting wave–current interactions. This configuration has been shown to reproduce realistic wave-in-ice behaviour in the Barents and Beaufort Seas (Ardhuin et al., 2018) and yields MIZ extents consistent with ICESat-2 altimeter observations (Boutin et al., 2022). ~~Boutin et al. (2021) used this coupled systemto investigate changes in sea ice dynamics and deformation, and we extend its application to the upper ocean mixing. Specifically, we quantify surface friction velocity and Stokes drift to derive LT metrics under varying sea ice and wave conditions. By resolving both the mechanical feedback from wave radiation stress (Longuet-Higgins and Stewart, 1962) and the impact of floe fragmentation on wave energy dissipation, the model provides a physically consistent framework for estimating LT mixing potential across the Arctic (Van Roekel et al., 2012; Li et al., 2017, 2019).~~

~~Our simulation spans the period~~ Our simulations cover the pan-Arctic domain for 2018~~–~~2022~~over a pan-Arctic domain with 25 km nominal resolution. The sea ice~~ , with three-hourly output from the coupled neXtSIM–WW3 model. This framework does not include a prognostic ocean mixed layer, surface waves do not feed back on stratification or vertical redistribution of turbulence. All Langmuir-related metrics presented here therefore represent the potential for mechanically forced Langmuir turbulence implied by surface forcing, rather than the fully realized upper-ocean response. The oceanic stratification and mixed layer depth (MLD) used in subsequent energetic diagnostics are prescribed independently from the GLORYS12V1 reanalysis, rather than evolving prognostically within the coupled system. This analysis thus quantifies the spatial structure of Langmuir-driven mixing implied by surface forcing alone. This definition is analogous to the Langmuir forcing framework

of Li et al. (2019) and captures relative patterns of Langmuir activity even when absolute dissipation rates are not explicitly resolved.

The coupled model provides key advantages over methods that only combine sea ice fields with ERA5 waves or rely on empirical Stokes drift formulations (Webb and Fox-Kemper, 2011). In neXtSIM–WW3, Stokes drift and ~~wave models exchange information every 30 minutes, and output is recorded every 3 hours. NeXtSIM receives oceanic boundary conditions from the GLORYS12 reanalysis and uses~~ wave radiation stress are computed directly from the ice-attenuated wave spectrum, rather than assuming open ocean conditions. Moreover, the prognostic FSD in neXtSIM modulates wave attenuation in a physically consistent manner, allowing the wave field to respond to floe fragmentation and the evolving seasonal morphology of the ice cover. By contrast, ERA5 ~~for atmospheric forcing (Hersbach et al., 2020)~~treats sea ice as land above a concentration threshold and therefore cannot capture attenuation, directional filtering, or the associated modulation of Stokes drift, processes that exert strong control on Langmuir forcing in the MIZ. Both models use the same physical parameters as the ~~REF~~ reference configuration described in Boutin et al. (2022). ~~Appendix A (Table A1)~~ Table S1 in the Supplementary Material lists the wave, wind, sea ice, and surface ocean variables used in this study, either directly from model output or computed from established physical relationships.

1.1 ~~Surface Stress Partitioning and Wind–Wave Forcing~~Evaluation of model inputs relevant to LT metrics

To assess the fidelity of the neXtSIM–WW3 inputs most relevant for LT diagnostics, we evaluate the surface winds, surface shear, Stokes drift, and the representation of heterogeneous sea ice and MIZ conditions. ERA5 winds, which force both neXtSIM and WW3, exhibit increased uncertainty under strong wind and high-latitude conditions, particularly near sharp ice–open-water transitions. Consistent with this, comparison against Cross-Calibrated Multi-Platform (CCMP) v3.1 data shows that ERA5 winds are systematically weaker than satellite-derived winds, and that this bias propagates directly into the diagnosed friction velocity u_*. Over 2018–2022, area-weighted Arctic mean 10-m winds exhibit a mean bias of -1.46 m s^{-1} (ERA5–CCMP), an RMSE of 1.47 m s^{-1}, and a correlation of 0.99 (Fig. S1), indicating high fidelity in synoptic variability despite a low mean state bias. Because CCMP assimilates ERA5 as a background field, this comparison primarily constrains mean state uncertainty.

The fidelity of neXtSIM sea ice concentration, ice-edge location, and deformation has been demonstrated in multiple studies. Ólason et al. (2025) report pan-Arctic sea ice extent RMSE of 0.76×10^6 km^2 and show that neXtSIM reproduces observed patterns of ice drift and deformation from OSI-SAF products, supporting its ability to represent heterogeneous ice fields that modulate wave penetration and Stokes drift pathways.

Accurate estimation of Stokes drift $u_{s(0)}$ further depends on realistic representation of short-wave attenuation in ice. The IS2+IC2 attenuation scheme implemented in WW3 has been shown to reproduce observed wave decay and spectral evolution in the Beaufort MIZ (Ardhuin et al., 2018), and to yield realistic pan-Arctic MIZ extents and wave-affected ice regimes consistent with ICESat-2–derived freeboard variability and floe-scale ice properties (Boutin et al., 2022). Based on sensitivity analyses and independent observational constraints, prior studies indicate that residual uncertainty in the short-wave spectrum, and

hence in inferred Stokes drift, is dominated by uncertainties in wind forcing and sea ice concentration, with magnitude on the order of tens of percent rather than order-unity errors (Ardhuin et al., 2018; Boutin et al., 2022).

1.2 Surface stress partitioning and wind–wave forcing

To characterize momentum input into the ocean mixed layer under partial ice cover, we compute an effective surface stress that accounts for both the stress transmitted through both sea iceand the direct wind stress over open waterpartitions momentum between the ice–ocean and atmosphere–ocean interfaces. Following the stress partitioning framework of Brenner et al. (2021), the net ocean surface stress is defined as an area-weighted combination of ice–ocean and atmosphere–ocean stresses, scaled by the local sea ice concentration:

$$\tau\boldsymbol{\tau}_{ocn} = A\tau\boldsymbol{\tau}_{io} + (1-A)\tau\boldsymbol{\tau}_{ao} \tag{1}$$

where A is the sea ice concentration (0 = open ocean, 1 = fully ice-coveredice covered), and the direct atmosphere-ocean stress , is : atmosphere–ocean stress is given by:

$$\tau\boldsymbol{\tau}_{ao} = \rho_a C_{ao}|\,|\mathbf{u}_a|\,|\mathbf{u}_a \tag{2}$$

with ρ_a with ρ_a as air density, $\mathbf{u}_a$ the 10-m wind velocity, and C_{ao} C_{ao} the air–sea drag coefficient over open water. In our configuration, the atmosphere–ocean stress is parameterized using Equation 2, while the ice–ocean stress (τ_{io}) is diagnosed directly from the neXtSIM sea ice model, based on the momentum transfer between sea ice and the underlying ocean. Although the neXtSIM-WW3 model setup does not include interactive ocean dynamics, it captures the surface forcing of momentum pathways which drives turbulence in the OSBL.

Subsequently, we define the effective an effective water-side friction velocity u_*, which represents the shear strength at the ocean surface associated with the net surface stress transmitted to the ocean under partial ice cover:

$$u_* = \sqrt{\frac{|\tau_{ocn}|}{\rho_o}}\sqrt{\frac{|\boldsymbol{\tau}_{ocn}|}{\rho_o}}. \tag{3}$$

where ρ_o ρ_o is the density of seawater. It provides the fundamental scaling for wind-driven mixing processes. The net surface stress $\boldsymbol{\tau}_{ao}$ represents an upper bound on the momentum flux available to drive mixed-layer shear during periods of active wave growth. This primarily affects the absolute magnitude of the diagnosed friction velocity u_*, while its spatial structure and relative variability remain more robust.

In addition to wind shear, surface waves contribute momentum through Stokes drift, the net Lagrangian transport of water particles due to wave orbital motion. In WW3, the surface Stokes drift components (z = 0) are computed from the two-dimensional wave energy spectrum $F(k,\theta)$ as:

$$U_{sx}^{z=0} = g\int\int \frac{k^2\cos(\theta)}{\sigma^2} F(k,\theta)\,d\theta\,dk, \tag{4}$$

and

$$U_{sy}^{z=0} = g \int \int \frac{k^2 \sin(\theta)}{\sigma^2} F(k,\theta)\, d\theta\, dk. \tag{5}$$

~~where~~ Here, σ is the wave frequency, k is the wave number and θ the propagation direction. These expressions define the eastward and northward components of the surface Stokes drift vector u_s. The effective friction velocity and surface Stokes drift combined, provide ~~the necessary inputs for evaluating and understanding Langmuir-related mixing~~ two primary dynamical inputs required to evaluate *the potential for LT* under varying sea ice conditions.

1.3 Langmuir turbulence metrics in the Arctic

The Langmuir number (La_t) is a widely used parameter for quantifying the relative contributions of wind stress and wave-induced Stokes drift to upper ocean turbulence ~~(McWilliams et al., 1997)~~(McWilliams and Sullivan, 2000). It is defined as:

$$La_t = \sqrt{\frac{u_*}{u_{s(0)}}}, \tag{6}$$

where u_* is the friction velocity ~~derived from wind stress , and $u_{s(0)}$~~ associated with the effective surface stress applied to the ocean, and $u_{s(0)}$ is the surface Stokes drift magnitude. In the open ocean, typical values of La_t range between 0.2 and 0.5 (Belcher et al., 2012), suggesting strong wave influence and active Langmuir circulation development, although La_t can reach values near or above 1 when wave effects are weak and wind-driven processes dominate (McWilliams et al., 1997; Belcher et al., 2012). These ranges are consistent with results from LES and field observations showing that stronger LT and deeper mixing are associated with lower La_t (Harcourt, 2015). La_t is ~~thus widely~~ used in ocean modeling as a diagnostic of upper-ocean mixing regimes and to inform turbulence parameterizations. ~~Despite La_t being a standard metric for LT mixing potential, recent studies have proposed refined formulations that better reflect realistic ocean forcing conditions, particularly when wind and wave directions are misaligned (Kukulka et al., 2010; Van Roekel et al., 2012; Li and Fox-Kemper, 2017). Directional mismatches between the Stokes drift and wind stress can significantly reduce the effective wave contribution to Langmuir circulations~~However, the traditional formulation implicitly assumes that the wind stress and Stokes drift are aligned. In realistic wave fields, especially in the ~~presence of swell, variable winds, or broad directional wave spectra.~~ Arctic, where mixed swell, turning winds, and ice-induced attenuation are common, misalignment can strongly reduce the effective Stokes shear that drives Langmuir circulations (Kukulka et al., 2010; Van Roekel et al., 2012; Li and Fox-Kemper, 2017).

To account for ~~this, we also compute the projected Langmuir number (La_{proj}) as a supplementary diagnostic following (Van Roekel et al., 2012):~~ wind–wave misalignment, we adopt the *projected* Langmuir number of Van Roekel et al. (2012), which incorporates the dynamic orientation of the dominant Langmuir cells. In this framework, Langmuir cells do not necessarily align with the wind, but with the direction of maximum Lagrangian shear, set by a balance between Eulerian shear, Stokes drift, stratification, and Coriolis rotation. The dynamic orientation angle α_L represents the direction of the dominant Langmuir cells relative to the

wind. Incorporating this angle yields the generalized projected Langmuir number:

$$La_{\text{proj}} = \sqrt{\frac{|\mathbf{u}_*|}{|\mathbf{u}_{s(0)}|\cos(\theta_{\text{ww}})}}_{\text{proj}} \equiv \left(\frac{|u_*|\cos(\alpha_L)}{|u_{s(0)}|\cos(\theta_{ww}-\alpha_L)}\right)^{1/2}, \tag{7}$$

~~where θ_{ww}~~ where θ_{ww} is the angle between the wind stress and Stokes drift vectors. ~~This formulation projects the Stokes drift onto the wind direction, isolating the component that constructively interacts with~~ Equation (7) captures two effects: (i) the reduced wind-driven ~~shear to generate Langmuir circulations. In theory, this projection should ideally account for the dynamic orientation of Langmuir cells (α_L), which has been shown to vary between the wind and wave directions depending on wave age, stratification, and Coriolis effects (Van Roekel et al., 2012; Li et al., 2017). However, given the spatial~~ shear along the Langmuir cell axis via $\cos(\alpha_L)$, and (ii) the projected of Stokes forcing along that same axis via $\cos(\theta_{ww}-\alpha_L)$.

Direct evaluation of α_L requires resolving the vertical structure of the Lagrangian shear, which is not feasible at the ~ 25 km resolution of our ~~model ($\tilde{2}5$ km) , we cannot resolve the vertical shear structure required to estimate (α_L) reliably. We therefore adopt the simplifying assumption $\alpha_L = 0$, treating θ_{ww}(the wind–wave angle) as the effective misalignment . As a result, even La_{proj} may overestimate the suppression of LT in cases where the actual Langmuir cell alignment lies between wind and wave directions. Thus, La_{proj} functions as an upper-bound estimate for directional suppression of wave influence on LT, providing valuable insight into the sensitivity of LT potential to wind–wave misalignment under mixed forcing conditions.~~ pan-Arctic model. We therefore use the low-order wave (LOW) approximation α_{LOW} proposed by Van Roekel et al. (2012), which provides an empirical estimate of Langmuir cell orientation by combining Eulerian shear and surface-layer Stokes shear:

$$\tan\alpha_{\text{LOW}} \approx \frac{\langle \partial v_s/\partial z\rangle_{D_L}}{\langle -u_*/(\kappa z) + \partial u_s/\partial z\rangle_{D_L}}, \tag{8}$$

where angle brackets denote a depth average over the Langmuir-affected layer D_L, and κ is the von Kármán constant. LES results show that α_{LOW} captures the orientation of Langmuir cells over a wide range of wind–wave misalignment angles, making it suitable for large-scale applications.

1.3.1 ~~Langmuir Turbulence Energetics in the Arctic~~

~~To evaluate the impact of LT on upper-ocean energetics, we compute three diagnostics:~~ In situations with strong wind–wave misalignment, α_{LOW} typically reduces the effective projection of the ~~enhancement factor $\mathcal{E}$, the turbulent dissipation rate ε, and the mixed-layer-averaged vertical velocity variance $\langle w'^2\rangle_{H_{ML}}$. The LT enhancement factor $\mathcal{E}(La_{\bar{x}})$ quantifies the amplification of turbulence due to Langmuir circulation. This factor is derived as a function of the Langmuir number scalings $La_{\bar{x}}$, following the formulation of (Li et al., 2019):~~ Stokes drift into the Langmuir cell direction, partially counteracting the muted Langmuir response obtained when misalignment is represented solely by θ_{ww}. Hence, in our analysis, we we substitute α_{LOW} for α_L in Eq. (7), yielding

$$La_{\text{proj}} = \left(\frac{|u_*|\cos(\alpha_{\text{LOW}})}{|u_{s(0)}|\cos(\theta_{ww}-\alpha_{\text{LOW}})}\right)^{1/2}. \tag{9}$$

1.3.1 Surface forcing metrics and mixing regime classification

We introduce two complementary metrics to evaluate the potential for LT under partial sea ice cover. The first evaluates how frequently surface forcing beneath sea ice resembles open-water conditions, based on exceedance metrics for surface stress and wave forcing. The second classifies near-surface ocean conditions into discrete mixing regimes based on the Langmuir number La_t and tracks transitions between these regimes over space and time.

We define exceedance metrics to quantify how often the near-surface wind and wave forcing in ice-covered regions approaches values typical of open water. The two primary LT drivers considered are the surface friction velocity (u_*) and the surface Stokes drift velocity ($u_{s(0)}$). For each season (s) and grid cell (x, y), we define an open-water (OW) benchmark by computing the median value of a given variable X over all ice-free conditions (SIC < 0.15):

$$X_{\mathrm{OW}}^{(s)} = \mathrm{median}\{X_t(x,y) \,:\, \mathrm{SIC}_t(x,y) < 0.15,\ t \in s\}. \tag{10}$$

This benchmark represents the typical magnitude of atmosphere–ocean or wave-induced surface forcing under ice-free conditions during a given season.

At each ice-covered grid cell (SIC ≥ 0.15), we compute the fraction of time steps for which the local value exceeds the seasonal OW benchmark. For a single variable, the exceedance metric is defined as

$$\mathrm{Exceedance}_X^{(s)}(x,y) = \frac{N_t\left[\mathrm{SIC}_t(x,y) \geq 0.15 \ \wedge\ X_t(x,y) \geq X_{\mathrm{OW}}^{(s)}\right]}{N_t\left[\mathrm{SIC}_t(x,y) \geq 0.15\right]}, \tag{11}$$

where $N_t[\cdot]$ denotes the number of seasonal time steps satisfying the specified condition. Seasons follow meteorological definitions: winter (DJF), spring (MAM), summer (JJA), and fall (SON).

To isolate conditions most relevant for Langmuir turbulence, we further define a joint exceedance metric that quantifies the fraction of ice-covered time during which both surface friction velocity and surface Stokes drift simultaneously exceed their respective OW seasonal medians:

$$\mathcal{E}\,\mathrm{JointExceedance}^{(s)}(La_x x, y) \equiv \mathcal{E} = \cos\theta_{ww}\sqrt{1 + (c_1 La_x)^{-2} + (c_2 La_x)^{-4}}\,\frac{N_t\left[\mathrm{SIC}_t(x,y) \geq 0.15 \ \wedge\ u_{*,t}(x,y) \geq u_{*,\mathrm{OW}}^{(s)} \ \wedge\ u_{s(0),t}(x,\right.}{N_t\left[\mathrm{SIC}_t(x,y) \geq 0.15\right]} \tag{12}$$

~~where θ_{ww} is the angle between wind and Stokes drift directions and c_1~~ These exceedance metrics provide a physically interpretable measure of the frequency and persistence of LT-relevant surface forcing in ice-covered regions, relative to open-ocean benchmarks.

To characterize the evolving balance between wind-driven and ~~c_2 are empirical constants. Following (Van Roekel et al., 2012), we adopt $c_1 = 3.1$, $c_2 = 5.7$, and $\theta_{ww} = 0$ for La_t, and $c_1 = 3.1$, $c_2 = 5.4$ for La_{proj}. The enhancement factor is used to scale~~

~~the TKE dissipation rate, estimated as~~ wave-driven mixing, we classify surface forcing into three distinct regimes based on the turbulent Langmuir number La_t (Li et al., 2019). At each time step T and grid cell (x,y), the regime is defined as:

$$\mathcal{R}(x,y,T) = \begin{cases} 1 & \text{if } La_t(x,y,T) > 0.94 \quad \text{(Shear-dominated)} \\ 2 & \text{if } 0.43 < La_t(x,y,T) \leq 0.94 \quad \text{(Mixed-forcing)} \\ 3 & \text{if } La_t(x,y,T) \leq 0.43 \quad \text{(Wave-dominated).} \end{cases} \tag{13}$$

To relate mixing regimes to sea ice conditions, we define spatial regions $\Omega(T)$ at each time step based on the local sea ice concentration $\mathrm{SIC}(x,y,T)$:

$$\Omega_{\mathrm{ice}}(T) = \{(x,y) \,|\, \mathrm{SIC}(x,y,T) > 0.8\}, \tag{14}$$

$$\Omega_{\mathrm{MIZ}}(T) = \{(x,y) \,|\, 0.15 \leq \mathrm{SIC}(x,y,T) \leq 0.8\}, \tag{15}$$

$$\Omega_{\mathrm{OW}}(T) = \{(x,y) \,|\, \mathrm{SIC}(x,y,T) < 0.15\}. \tag{16}$$

For each region Ω and regime $r \in \{1,2,3\}$, we compute the spatial fraction of grid cells occupying regime r at time T as

$$\varepsilon f_r^{\Omega}(T) = \frac{u_*^3}{h} \mathcal{E} \frac{1}{|\Omega(T)|} \sum_{(x,y)\in\Omega(T)} \delta\Big(\mathcal{R}(La_x,x,y,T) = r\Big), \tag{17}$$

where ~~u_* is the friction velocity, h is the MLD, and ε represents the rate at which TKE is dissipated (W/kg). This formulation is based on empirically derived scaling relationships between Langmuir number and turbulence dissipation, developed primarily through LES studies (Van Roekel et al., 2012; Li et al., 2016, 2019). These relationships form the basis for parameterizing wave-driven turbulence enhancement in ocean models, including implementations within the K-Profile Parameterization (KPP) scheme (Li and Fox-Kemper, 2017). This framework accounts for surface waves providing an additional energy source for turbulence in the upper ocean boundary layer, thereby increasing dissipation rates relative to wind-only forcing~~ $\delta(\cdot)$ is the indicator function and $|\Omega(T)|$ is the number of valid grid cells in region $\Omega(T)$.

~~For additional calculations, we decompose the TKE dissipation into wind shear- and wave-driven contributions. Shear-driven dissipation is estimated as:~~

$$\varepsilon_{\mathrm{shear}} = u_*^3/\mathrm{MLD}$$

Beyond regime occupancy, we assess the temporal stability of the surface forcing balance by tracking transitions between regimes. For each grid cell (x,y), we count transitions from regime r_n to r_m between successive time steps, restricted to periods when the grid cell remains within the same ice regime Ω:

$$T^{\Omega}_{r_n \to r_m}(x,y) = \sum_{T=2}^{T_{\max}} \delta(\mathcal{R}(x,y,T-1) = r_n)\, \delta(\mathcal{R}(x,y,T) = r_m)\, \delta((x,y) \in \Omega(T-1) \cap \Omega(T)). \tag{18}$$

representing turbulence generated purely by wind-induced surface stress. Wave-induced effects are incorporated using $\mathcal{E}(La_x)$. The total dissipation is therefore given by:

$$\varepsilon_{\text{total}} = \varepsilon_{\text{shear}} \cdot \mathcal{E}(La_x)$$

and the Langmuir-induced component is calculated as:

$$\varepsilon_{\text{LT}} = \varepsilon_{\text{total}} - \varepsilon_{\text{shear}} = \varepsilon_{\text{shear}}(\mathcal{E}(La_x) - 1)$$

This formulation ensures that wind- and wave-driven mixing are explicitly separated, with ε_{LT} capturing only the wave-enhanced turbulence component. Thus, $\varepsilon_{\text{shear}}$ reflects baseline mixing from wind forcing alone, while ε_{LT} isolates the additional turbulent energy inputattributable to wave–wind interactions via LT Spatial differences in temporal sampling are evaluated using transition counts, normalized by the number of time steps a grid cell resides within region Ω,

$$\bar{T}^{\Omega}_{r_n \to r_m}(x,y) = \frac{T^{\Omega}_{r_n \to r_m}(x,y)}{N_{\Omega}(x,y)}, \tag{19}$$

where $N_{\Omega}(x,y)$ denotes the total number of time steps satisfying the regional criterion. The resulting normalized transition frequency provides a measure of how often the dominant surface forcing balance reorganizes at a given location over the analysis period.

To estimate the vertical component of turbulent motions, we adopted the empirical relationship developed by (Van Roekel et al., 2012) , which relates mixed-layer-averaged vertical velocity variance $\langle w'^2 \rangle_{H_{ML}}$ to the surface friction velocity, wind

1.3.2 Langmuir Turbulence Energetics

To examine how LT modifies upper-ocean energetics, we evaluate two complementary metrics derived from the vertically integrated turbulent kinetic energy (TKE) budget: (i) the mixed-layer–wave alignment, and the Langmuir number: averaged vertical velocity variance, $\langle w'^2 \rangle_{H_{ML}}$, and (ii) the TKE dissipation rate, ε. Both are based on empirically derived LES scalings, but they characterize distinct aspects of the turbulent response.

We compute $\langle w'^2 \rangle_{H_{ML}}$ following the LES-based scaling of Van Roekel et al. (2012):

$$\langle w'^2 \rangle_{H_{ML}} = 0.6 \left[u_* \cos(\theta_{ww} \alpha_{\text{LOW}}) \right]^2 \left(1 + (c_1 La_x)^{-2} + (c_2 La_x)^{-4} \right), \tag{20}$$

where u_* is the friction velocity and La_x denotes the Langmuir number metric used in the scaling. The La_x^{-2} and La_x^{-4} terms capture the nonlinear enhancement of vertical velocity variance by Langmuir forcing, with lower Langmuir numbers indicating stronger turbulence. The projection factor $\cos(\alpha_{\text{LOW}})$ ensures that vertical velocity is appropriately scaled along the Langmuir cell axis. For the turbulent Langmuir number, we set $La_x = La_t$ and $\alpha_{\text{LOW}} = 0$, corresponding to Langmuir cells aligned with the wind. We adopt $(c_1, c_2) = (3.1, 5.7)$ for La_t and $(c_1, c_2) = (3.1, 5.4)$ for La_{proj}, consistent with the original LES fits following Van Roekel et al. (2012). The scaling in Eq. (20) was derived under conditions of weak or destabilizing

surface buoyancy flux in LES. Because Arctic mixed layers are frequently stabilized by ice melt and freshwater input, the diagnosed values of $\langle w'^2 \rangle_{H_{ML}}$ should be interpreted as a measure of LT potential, rather than as a direct prediction of the realized turbulent state.

~~Here, $\langle w'^2 \rangle_{H_{ML}}$ is the vertical velocity variance averaged over the mixed layer, u_* is~~ The contribution of LT to upper-ocean energy dissipation is quantified using a vertically integrated turbulent kinetic energy (TKE) scaling framework following Belcher et al. (2012). In the mixed-layer interior, away from the near-surface wave-breaking region, the ~~friction velocity, and θ_{ww} is the angle between wind and Stokes drift directions. The parameter~~ turbulent dissipation rate can be approximated as the sum of contributions from wind-driven shear, Stokes drift (Langmuir turbulence), and surface buoyancy forcing. Factoring out the shear-based velocity scale yields:

$$\varepsilon \sim \frac{u_*^3}{H_{\mathrm{ML}}} \left[A_s + A_L \, La_x^{-2} + A_c \, \frac{B_s H_{\mathrm{ML}}}{u_*^3} \right], \tag{21}$$

where H_{ML} is the mixed-layer depth, La_x is ~~the Langmuir scaling, and c_1 and c_2 are the same empirical constants used in Equation 8, following Van Roekel et al. (2012).This definition accounts for the nonlinear amplification of vertical motions associated with LT~~a Langmuir number metric characterizing the relative importance of wave forcing to shear, and B_s is the surface buoyancy flux. The constants A_s, ~~with enhancement increasing as La_x decreases. To assess the influence of wave–ice interactions and wave –wind directional misalignment, we compute all energetic estimates using both La_t and La_{proj}. To estimatedissipation and VKE from LT~~A_L, and A_c are empirical coefficients of order unity that represent the efficiency of shear-, Langmuir-, and buoyancy-driven turbulence, respectively.

The Langmuir contribution in Eq. (21) scales as La_x^{-2}, reflecting the ratio of the Stokes drift velocity scale to the friction velocity, u_s/u_*. This scaling is consistent with the Langmuir velocity scale $w_{*L} = (u_*^2 u_s)^{1/3}$ and with LES results demonstrating enhanced interior mixing under strong wind–wave coupling (Belcher et al., 2012; Van Roekel et al., 2012).

Consistent with the surface forcing-only framework described in Section 2.1, we omit the buoyancy-dependent contribution in Eq. (21) and adopt a reduced formulation that isolates mechanically driven turbulence. We define a mechanically forced dissipation scale as:

$$\varepsilon_{\mathrm{mech}} = \frac{u_*^3}{H_{\mathrm{ML}}} \left(1 + \beta \, La_x^{-2}\right), \tag{22}$$

where the second term represents enhancement of turbulent dissipation by wave-induced Stokes drift. The empirical coefficient β parameterizes the efficiency with which LT augments mechanically driven dissipation under weakly stratified conditions. LES in open-ocean settings suggest $\beta \approx 0.15$. We emphasize that $\varepsilon_{\mathrm{mech}}$ is an energetic proxy rather than a full representation of turbulent dissipation, as it neglects buoyancy production, entrainment, and stratification-dependent suppression. Its purpose here is to quantify the spatial and temporal variability of mechanically mediated energy input associated with wind and wave forcing, providing a physically interpretable metric for comparing mixing regimes within the MIZ.

We adopt a reanalysis-derived mixed-layer depth H_{ML} as a physically consistent bulk depth scale rather than a real-time boundary-layer estimate. Specifically, we use ~~MLD data available from the GLORYS12V1 reanalysis (produced by Mercator Ocean for Copernicus Marine Service), which provides daily~~ , the GLORYS12 reanalysis (0.08° ~~resolution global ocean fields. The MLD is defined using a potential density threshold criterion ($\Delta\sigma_\theta = 0.03\,\mathrm{kg\,m^{-3}}$ from surface) (Copernicus Marine Service, 2020) , consistent with standard practice and well suited for capturing seasonal and regional stratification associated with freshwater input in the Arctic Ocean. However, this is not a prognostic variable responding dynamically to surface wave or wind forcing within our coupled model. Instead, it provides a diagnostic estimate of stratification depth, which we use to contextualize LT-driven turbulence under realistic hydrographic constraints.~~ ° resolution), computed daily and remapped to the 25 km model grid. Although GLORYS12 does not explicitly resolve ice-modified boundary-layer processes, its mixed-layer depth provides a physically grounded, spatially and seasonally varying vertical scale over which mechanically forced turbulence can be interpreted in a vertically integrated sense. Equation (22) is therefore interpreted as an effective dissipation scaling rather than a closed TKE budget, and is used here as a diagnostic of LT potential under wind–wave forcing.

~~Summary of Langmuir Turbulence Diagnostics and Scalings~~

2 Results

2.1 Spatiotemporal variability of surface forcing across the Arctic

~~We introduce a metric to assess how often local conditions under ice resemble those in open water~~ Figure 1 presents the seasonal distribution of joint exceedance of open-water (OW)~~, allowing us to evaluate the occurrence and intensity of surface forcing relevant to LT in ice-covered regions. We focus on three key variables: surface friction velocity (u_*), surface Stokes drift velocity ($u_{s(0)}$), and significant wave height (h_s). For each grid cell (x, y) and season, we compute the fraction of time steps during which a variable X (u_*, $u_{s(0)}$, or h_s) in ice-covered conditions (SIC ≥ 0.15) exceeds the seasonal median of the same variable calculated over OW conditions (SIC < 0.15) across the Arctic domain. This results in a spatially resolved indicator of how often local forcing under sea ice reaches or surpasses levels typically observed in open water:~~ -like surface forcing over the five-year simulation period. Across all seasons, joint exceedance is generally low, with values rarely exceeding 0.2, indicating that conditions comparable to OW, where strong winds and waves act simultaneously, occur only infrequently in sea ice. Where it does occur, joint exceedance is spatially confined and predominantly concentrated along the seasonal sea ice edge. The highest values are consistently found in the Barents, Greenland, and Chukchi Seas, regions where ice cover is thinner, more mobile, and more frequently disrupted.

$$\mathrm{OW\_Exceedance}_{\mathrm{ice}}(x,y) = \frac{N_t\left[\mathrm{SIC}_t(x,y) \geq 0.15 \wedge X_t(x,y) \geq X^{(s)}_{\text{median-OW}}\right]}{N_t\left[\mathrm{SIC}_t(x,y) \geq 0.15\right]}$$

~~where $X^{(s)}_{\text{median-OW}}$ is the seasonal median computed over all open-water grid cells and $N_t[\cdot]$ counts the number of time steps satisfying the condition. Seasons were defined using meteorological groupings: DJF (Dec–Feb), MAM(Mar–May), JJA~~

(Jun–Aug), and SON (Sep–Nov), assigned based on the month of each time point in The spatial distribution exhibits clear seasonal contrasts. During winter and the dataset. transitional seasons (DJF, MAM, SON), joint exceedance is stronger and more spatially continuous along the MIZ, reflecting the increased likelihood of storm-driven conditions interacting with loosely consolidated ice. In contrast, summer (JJA) shows the weakest joint exceedance overall. However, exceedance events in summer are more geographically dispersed, suggesting that while LT-relevant forcing is rarer, it can still intermittently extend into areas classified as pack ice. This scattered summer signal highlights the potential for episodic Langmuir turbulence beyond the immediate MIZ during the melt season.

The distribution of u_* is narrowly centered around $\sim 0.01\ m/s$, with minimal seasonal variability (Figure 1a) , suggesting relatively consistent wind-driven shear stress across the year in the OW To provide additional physical context for this seasonal asymmetry, Supplementary Figure S2 summarizes the distribution of significant wave height (H_s) within the marginal ice zone (MIZ) across seasons. Winter (DJF) exhibits both the highest median wave heights and the largest spread, consistent with frequent storm-driven wave events capable of penetrating into partially ice-covered regions. In contrast, $u_{s(0)}$ is centered around $\sim 0.1\ m/s$ and exhibits stronger seasonality (Figure 1b) , summer (JJA) wave heights are strongly suppressed, with low median values and limited variability, consistent with reduced Stokes drift forcing even where ice cover is fragmented. The transitional seasons (MAM, SON) exhibit intermediate behavior, characterized by lower median wave heights but pronounced upper tails, reflecting episodic wave events rather than sustained wave forcing.

Consistent with seasonal wave climate, the confinement of joint exceedance to the MIZ across all seasons highlights the role of sea ice state in regulating surface forcing. Reduced joint exceedance during summer reflects both diminished storm activity and enhanced attenuation of wave-induced Stokes drift within even moderately concentrated ice, in agreement with elevated values during winter months and reduced values in summer. The h_s distribution spans a broader dynamic range, with higher seasonal means and medians in winter (Figure 1c) , reflecting increased wave activity during this period. Figures 1d-f, show the spatial distribution of OW exceedance frequencies within the ice-covered Arctic (SIC ≥ 0.15) . The exceedance map for u_* reveals widespread regions, extending deep into the MIZ and central Arctic, where local shear often matches or exceeds OW medians. High exceedance rates are particularly pronounced in the Barents, Laptev, and Chukchi Seas and in Davis Strait. This indicates that atmospheric momentum can continue to penetrate efficiently through the sea ice cover across extensive areas of the Arctic. It supports the hypothesis proposed by Martin et al. (2014, 2016), who argued that momentum transmission through sea ice can be regionally and seasonally enhanced when internal ice stress is low. In loosely packed - mobile ice, wind coupling to the ocean can remain strong or even be enhanced relative to OW. In contrast, exceedance frequencies for $u_{s(0)}$ are essentially zero, indicating that Stokes drift is heavily suppressed beneath sea icedue to wave attenuation and scattering processes (Ardhuin et al., 2016). This suppression is consistent with theoretical and observational studies showing that the Stokes transport rapidly decays under even documenting rapid decay of Stokes transport under partial ice cover (Ardhuin et al., 2016; Herman, 2017; Liu and Mollo-Christensen, 1988). Despite the lack of $u_{s(0)}$ exceedance (Ardhuin et al., 2016; Herman, 2017; Liu and Mollo-Christensen, 1988). In contrast, the persistence of joint exceedance during winter and transitional seasons indicates that episodic storm-driven events can temporarily restore OW-like forcing beneath the ice, h_s shows notable exceedance frequencies, primarily concentrated along the seasonal iceedge. This

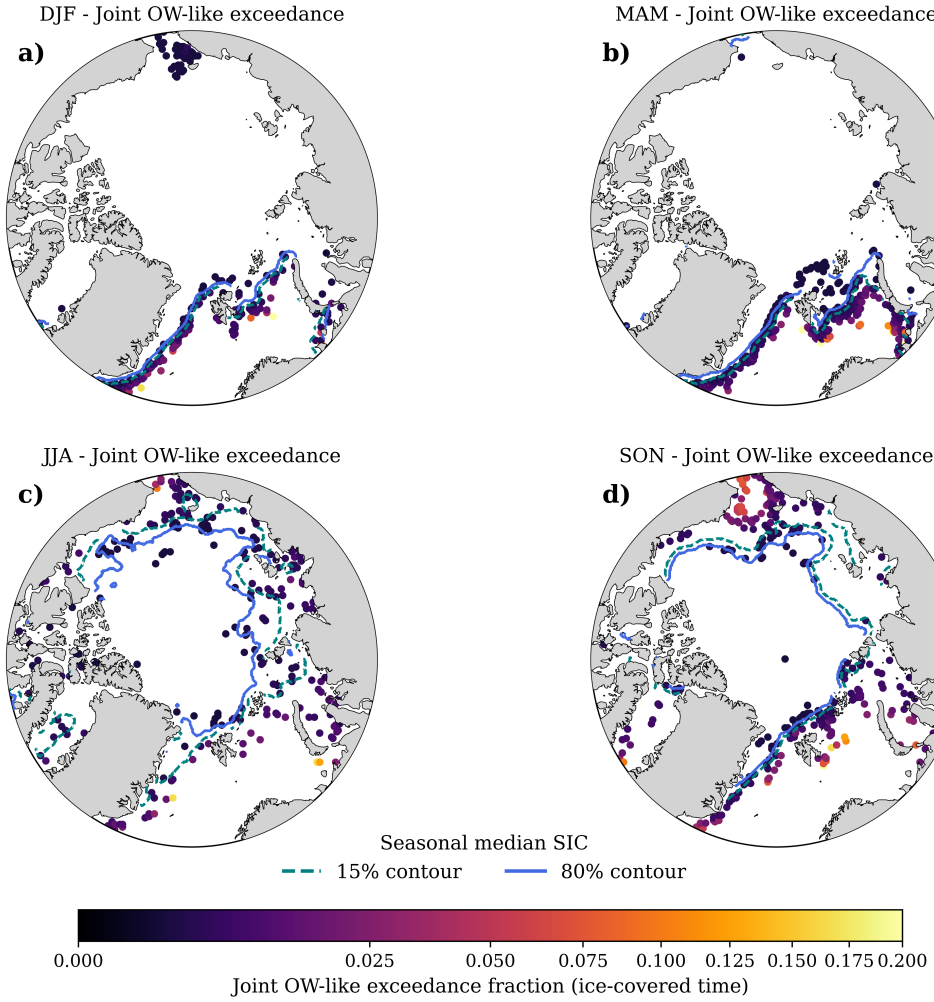

Figure 1. **Seasonal joint exceedance of wind–wave surface forcing beneath Arctic sea ice.** Panels (a–d) show, for each season, the fraction of under-ice time ($SIC \geq 0.15$) during which both surface friction velocity u_* and surface Stokes drift $u_{s(0)}$ simultaneously exceed their respective seasonal open-water medians ($SIC < 0.15$). Elevated values (yellow–orange) indicate locations where wind-driven shear and residual wave-driven drift intermittently reach open-water–like magnitudes despite the presence of sea ice. A nonlinear (power-law) color scaling is applied to enhance contrast at low exceedance fractions, emphasizing spatial variability in rare joint exceedance events. Dashed and solid contours denote the seasonal mean **15%** (teal) and **80%** (blue) sea ice concentration boundaries, respectively, providing context for the typical extent of the marginal ice zone and the transition to the consolidated pack. Joint exceedance is shown only at grid cells that experience sea ice conditions at least once during each season.

~~suggests that surface waves are capable of penetrating into partially ice-covered areas, particularly near dynamic or retreating ice margins (Thomson et al., 2018). Localized wave presence, highlights the spatially constrained but temporally episodic nature of wave-driven processes in the Arctic MIZ. The contrast between the widespread exceedance of u_* and the confined nature of h_s exceedance, illustrates a key asymmetry in the surface forcing regime across the sea ice covered Arctic.~~ even when mean conditions remain ice covered.

~~Seasonal distribution and under-ice exceedance of surface friction velocity (u_*), surface Stokes velocity (u_s) and significant wave height (h_s) in the Arctic.~~ ~~(a, b, c) Seasonal histograms of u_*, $u_{s(0)}$, and h_s over OW grid cells ($SIC < 0.15$), with vertical lines marking the median (solid) and mean (dashed) for each season. (d, e, f) Fraction of time steps under ice-covered conditions ($SIC \geq 0.15$) where values of u_*, $u_{s(0)}$, and h_s exceed the seasonal median open water threshold. The dashed contour represents the median 80% SIC boundary, indicating the typical MIZ extent. Color scale denotes the frequency of exceedance (0 to 1), with high values indicating regions of frequent open-water-like behavior in sea ice covered regions.~~

~~The spatial distribution and seasonal evolution of the median Langmuir number (La_t) characterize dominant upper-ocean turbulent mixing regimes across the Arctic (Figure~~

2.2 Mapping upper-ocean mixing regime dynamics in the Arctic

To further explore the controls on LT potential, we examine the spatial and seasonal structure of the turbulent Langmuir number (La_t). All La_t medians are computed over the full spatial domain shown in Figure 2~~). In all seasons, elevated median La_t values (> 1.5~~, without restricting the analysis based on sea ice concentration. The five-year climatological median (Figure 2a) reveals a persistent band of low La_t encircling the perennial ice pack and closely following the climatological 15% SIC contour and consistent with patterns shown in Figure 1. Elevated median La_t values (> 1) dominate the central ~~ice-covered Arctic , indicating conditions~~ Arctic under compact ice cover, indicating regimes where wave influence ~~remains~~ is weak and surface shear ~~primarily governs~~ governs upper-ocean mixing. In contrast, ~~lower median La_t values (< 0.45~~moderate to low median La_t values (< 0.45), which ~~signal dynamically significant LT , appear in~~ indicate some LT potential, are confined to narrow, seasonally evolving bands along the ~~MIZ. These LT-favorable zones track the climatological ice edgeand expand in late summer and fall (Figure 2e), when open water exposure and increased wave activity enhance Stokes drift penetration. Spring and winter patterns (Figures 2b–c)exhibit sharp transitions between high and low La_t, showing how compact ice suppresses wave-driven mixing. The 5-year climatological median (Figure 2a) reveals a persistent band of low La_t encircling the perennial ice pack and closely tracking the 15% SIC contour. This alignment, shows that there is LT potential in the seasonal MIZ, and indicates the critical role of sea ice cover in modulating access to wave energy and, consequently, shaping the turbulent mixing regimes.~~

ice edge. Under open-ocean conditions (SIC < 0.15), median La_t values are generally below 0.35, consistent with the range identified by Belcher et al. (2012) as favorable for LT conditions. This large-scale spatial structure reflects the progressive suppression of wave-induced Stokes transport with increasing ice concentration, as LT potential diminishes when Stokes production weakens relative to shear production.

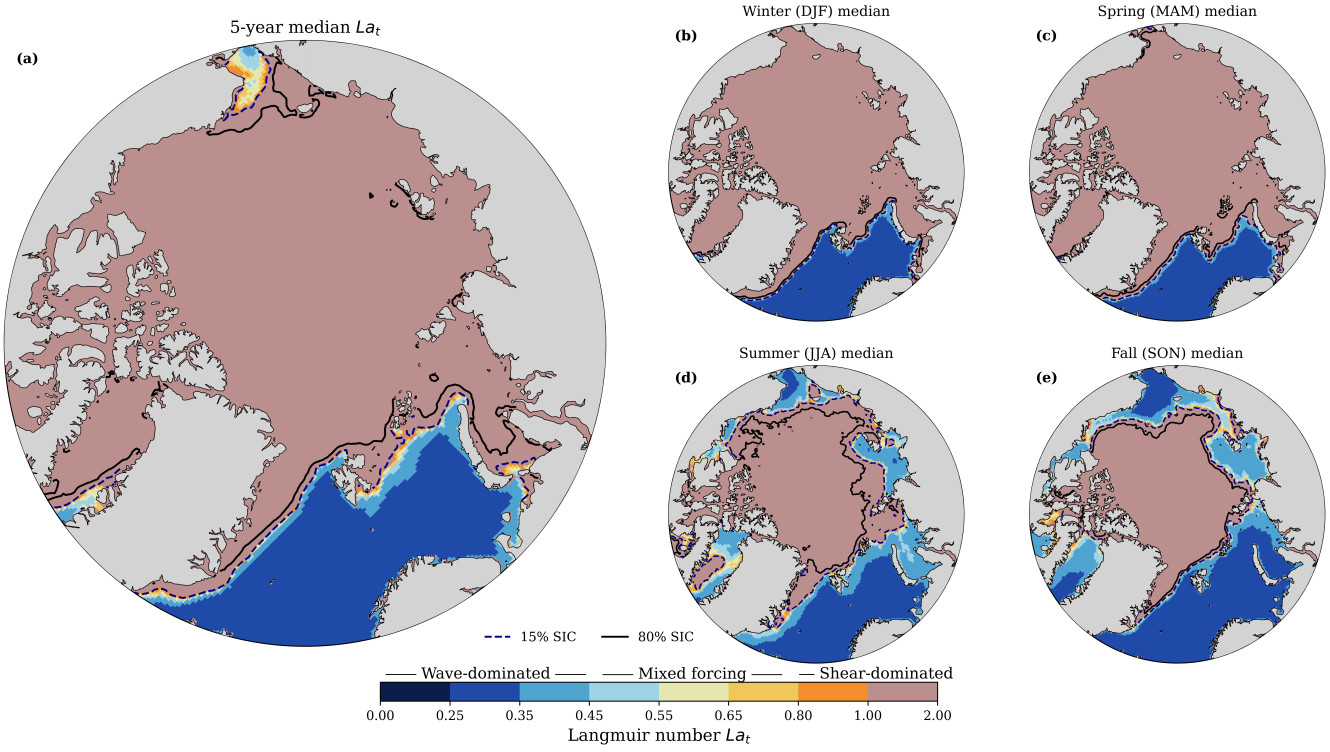

Figure 2. Spatial distribution of the median Langmuir number La_t, integrated over 2018 to 2022, along with its seasonal medians. Panel (a) ~~presents~~ shows the ~~overall~~ five-year climatological median of the Langmuir number La_t computed across all seasons. The median 15% and 80% SIC contours are overlaid in ~~black and~~ dark blue and black colors marking the median SIC-defined extent of the MIZ across seasons. Panels (b–e) show the medians for winter (DJF), spring (MAM), summer (JJA), and fall (SON), respectively. ~~The typical~~ In all panels, La_t ~~-active open~~ is shown for all ocean ~~and LT-weak thresholds~~ grid cells without applying a SIC mask; SIC contours are ~~also indicated on the color scale~~ overlaid for ~~reference~~context.

~~To further explain the seasonal controls on LT potential within the MIZ, we analyze the frequency of surface Stokes drift ($u_{s(0)}$) and friction velocity (u_*)exceedance across physically motivated thresholds. These thresholds correspond to varying regimes of wave-induced mixing intensity, ranging from weak wave influence to conditions strongly conducive to LT. A day is classified as a MIZ day if at least one grid cell satisfies the condition $0.15 \leq \mathrm{SIC} \leq 0.8$, ensuring that partial icecover and associated wave access are represented. Our findings, summarized in Figure A1, reveal that low-intensity surface Stokes drift forcing ($u_{s(0)} > 0.02\ \mathrm{m\,s^{-1}}$) is ubiquitous in winter (99.8% of MIZ days) and spring (98%), and remains substantial even in summer (71.7%) and fall (72.0%), showing that weak wave-driven turbulence is a persistent background feature of the MIZ, even during seasons with reduced wave activity. Moderate wave forcing ($u_{s(0)} > 0.05\ \mathrm{m\,s^{-1}}$), often associated with LT-active in prior studies, is similarly common in DJF (98%) and MAM (86%), but occurs on only 20.2% and 27.0% of MIZ days in JJA and SON, respectively. The occurrence of strong wave forcing($u_{s(0)} > 0.10\ \mathrm{m\,s^{-1}}$), corresponding to $La_t \approx 0.3 - 0.4$ and~~

indicative of enhanced LT potential, is seasonally skewed—observed on 85% of MIZ days in DJF and 58% in MAM, but only ~10% in~ Seasonal medians (Figures 2b–e) further illustrate how transitions in ice state modulate the balance between wave and wind forcing. During winter and spring (Figures 2b–c), sharp gradients in La_t delineate the transition from wave-influenced conditions near the ice edge to shear-dominated regimes within the consolidated ice. This abrupt shift reflects compact ice cover and strong wave attenuation, which limit Stokes drift penetration beneath the ice even during periods of strong wind forcing. In contrast, summer and fall ~~. Extreme events ($u_{s(0)} > 0.20\ \mathrm{m\,s^{-1}}$) , characteristic of storm-driven swell penetration or near ice-edge exposures, are rare in JJA and SON (<10%), though reach up to 43% in DJF.~~

~~Wind-driven shear emerges as a pervasive and seasonally consistent component of upper ocean forcing in the MIZ. Friction velocities exceeding $0.01\ \mathrm{m\,s^{-1}}$ occur on nearly all MIZ days throughout the year, indicating a persistent baseline for turbulence generation via wind stress. Moderate shear conditions ($u_* > 0.03\ \mathrm{m\,s^{-1}}$) are sustained during 44% of winter days and 30% of spring days, but their prevalence diminishes sharply in summer and fall to approximately 10%. Strong wind forcing ($u_* > 0.04\ \mathrm{m\,s^{-1}}$) remains infrequent, even in winter, where it occurs on just 6% of MIZ days. These patterns highlight a pronounced seasonal asymmetry in LT-relevant forcing, where wind stress offers a continuous, albeit variable, source of mechanical energy, while wave-driven enhancement is intermittent and strongly constrained~ (Figures 2d–e) exhibit a broader and more continuous band of reduced La_t extending into the seasonal sea ice zone. Increased OW exposure, enhanced fetch, and elevated wave activity during these seasons allow Stokes drift to penetrate farther beneath the ice, reducing La_t and promoting conditions more conducive to LT. These seasonal patterns indicate that departures from open-ocean La_t values are primarily associated with modulation of Stokes drift by sea ice ~~. The episodic nature of wave access, particularly during summer and autumn, restricts the occurrence of fully wave-dominated turbulence regimes. Even in OW, Langmuir numbers below 0.25, indicative of intense LT and wave-dominant mixing , are not common (Figure 2) , aligning with phase-space constraints previously identified by Li et al. (2019). As aresult, the prevailing state of turbulence within the MIZ is one of mixed forcing, characterized by intermediate Langmuir numbers ($0.35 \lesssim La_t \lesssim 1.5$). These values suggest a regime where LT is present but not dynamically dominant.~

2.3 ~~Mapping upper ocean mixing regime dynamics in the Arctic~

~~Several approaches have been developed to classify turbulence regimes in the OSBL, each emphasizing different regions of the non-dimensional parameter space defined by La_t. In the context of LT, LES studies have classified surface mixing regimes based on the relative contributions of wind shear and Stokes drift to TKE production and dissipation (e.g., Belcher et al., 2012; Li et al., 201 . Following the framework of Li et al. (2019), we adopt regime boundaries to distinguish between wave-dominated,~ rather than changes in wind forcing alone. The seasonal MIZ therefore emerges as a dynamically distinct transition zone in which the balance between shear- and wave-driven turbulence shifts toward LT-favorable conditions, while the interior pack ice remains characterized by persistently shear-dominated ~~, and mixed-forcing conditions. At~ mixing throughout the year.

2.3 Mapping upper-ocean mixing regime dynamics in the Arctic

Figure 3 synthesizes the spatial structure, temporal variability, and persistence of upper-ocean mixing regimes under consistent sea ice concentration ($SIC > 15\%$) conditions. Panel (a) shows the dominant mixing regime at each grid cell, defined by $\geq$50% seasonal persistence and quantified using Eq. (13). The Arctic interior is characterized primarily by shear-driven mixing ($La_t \geq 0.94$), while mixed ($0.43 \leq La_t < 0.94$) and wave-driven ($La_t < 0.43$) regimes are confined to the MIZ and regions proximal to the ice edge, where surface-wave and wind forcing increasingly compete. Panel (b) maps the normalized frequency of regime transitions at each grid cell~~location (x,y) and analysis time T, the local Langmuir number $La_t(x,y,T)$ is used to assign a mixing regime:~~

$$\mathcal{R}(x,y,T) = \begin{cases} 1 & \text{if } La_t(x,y,T) > 0.94 \quad \text{(Shear-dominated)} \\ 2 & \text{if } 0.43 < La_t(x,y,T) \leq 0.94 \quad \text{(Mixed forcing)} \\ 3 & \text{if } La_t(x,y,T) \leq 0.43 \quad \text{(Wave-dominated)} \end{cases}$$

~~To contextualize these regimes in relation to sea ice conditions~~, ~~we define spatial regions $\Omega(T)$ at each time step T based on the sea ice concentration $\mathrm{SIC}(x,y,T)$:~~

$$\Omega_{\mathrm{ice}}(T) = \{(x,y) \,|\, \mathrm{SIC}(x,y,T) > 0.8\}$$

$$\Omega_{\mathrm{MIZ}}(T) = \{(x,y) \,|\, 0.15 \leq \mathrm{SIC}(x,y,T) \leq 0.8\}$$

$$\Omega_{\mathrm{OW}}(T) = \{(x,y) \,|\, \mathrm{SIC}(x,y,T) < 0.15\}$$

~~For each region Ω and regime $r \in \{1,2,3\}$, we compute the spatial fraction of grid cells classified in regime r at time T as:~~

$$f_r^{\Omega}(T) = \frac{1}{|\Omega(T)|} \sum_{(x,y)\in\Omega(T)} \delta\left(\mathcal{R}(x,y,T) = r\right)$$

~~where $\delta(\cdot)$ is the indicator function (equal to 1 when the condition is true, 0 otherwise), and $|\Omega(T)|$ is the number of valid grid cells in region $\Omega(T)$.~~

~~For the regime transitions, we track changes in $\mathcal{R}(x,y,T)$ from one time step to the next. The number of transitions from regime r_n to r_m at location (x,y), restricted to grid cells within region Ω, is given by:~~

$$T_{r_n \to r_m}^{\Omega}(x,y) = \sum_{T=2}^{T_{\max}} \delta\left(\mathcal{R}(x,y,T-1) = r_n\right) \cdot \delta\left(\mathcal{R}(x,y,T) = r_m\right) \cdot \delta\left((x,y) \in \Omega(T-1) \cap \Omega(T)\right)$$

~~To account for differences in temporal sampling coverage across the domain, we normalize the transition count by~~ expressed as the number of regime changes per ice-covered day. Enhanced regime instability is strongly localized to the MIZ, particularly

along sectors exposed to episodic wave activity and intermittent open-water conditions. In contrast, the ~~number of time steps in which a grid cell lies within the region:~~

$$\bar{T}^{\Omega}_{r_n \to r_m}(x,y) = \frac{T^{\Omega}_{r_n \to r_m}(x,y)}{N_{\Omega}(x,y)}$$

~~where $N_{\Omega}(x,y)$ is the number of time steps in which (x,y) satisfies the condition defining region Ω. This normalization yields a dimensionless frequency in $[0,1]$ that reflects how often a specific regime transition occurs at each location over the analysis period.~~

consolidated interior pack ice exhibits uniformly low transition rates, indicative of stable and persistent forcing balances throughout the year. ~~Figure 3 shows how differences in wind and wave forcing, previously quantified using Equation 14, shape the dominant mixing regimes across the Arctic. In the open ocean, where waves are most accessible, La_t values frequently fall below 0.43, indicating wave-dominated turbulence. In the MIZ, a transitional region with variable sea ice concentration, mixing regimes more often fall within the mixed-forcing range $(0.43 < La_t \leq 0.94)$. Consistent with the suppressed Stokes drift found under sea ice , the majority of the interior Arctic exhibits persistently high $La_t > 0.94$, indicating that shear-driven mixing is the prevailing regime. This is reflected in panel (a) , where much of the central Arctic and parts of the seasonal ice pack are classified as shear-dominated over the five years of the analysis.~~

~~The seasonal cycle in panel (b) , highlights that the balance between wind-driven~~ The temporal evolution of regime instability within the MIZ is shown in panel (c), quantified as the fraction of MIZ grid cells ($0.15 \leq \text{SIC} \leq 0.8$) that undergo at least one regime transition within a 30-day window. Regime instability exhibits pronounced seasonal modulation, with recurrent peaks during periods of ice advance and retreat. Peaks in regime instability systematically precede maxima in MIZ area, indicating a temporal lag between dynamic reorganization and the geometric expansion of the SIC-defined MIZ. Periods of elevated instability correspond to times when grid cells reside near regime boundaries and experience strong competition between wind-, wave-, and ~~wave-driven turbulence is highly sensitive to sea ice concentration. Wave-influenced regimes grow in summer and early fall, as ice retreats and wave exposure increases, while shear-driven conditions dominate during winter and spring. Transitions between regimes, shown in panel (c), occur most frequently near the~~ ice-mediated forcing, whereas subsequent MIZ expansion reflects the integrated outcome of this reorganization. Panel (d) directly links regime instability to persistence by relating the mean time between regime transitions to the longest continuous duration of a single regime within MIZ grid cells. Median regime persistence increases monotonically with increasing time between transitions, however the relationship is highly non-linear, with persistence collapsing rapidly once transitions become more frequent. In our analysis, this collapse occurs at inter-transition timescales of order several weeks, although the precise threshold varies spatially across the MIZ. The broad interquartile range at short transition timescales reflects substantial variability associated with intermittently forced regimes near the ice ~~edge and shelf boundaries-regions also identified earlier as hotspots of mixed wind-~~ edge, whereas longer transition times are associated with sustained, dynamically stable regimes. Together, panels (c) and ~~wave- forcing . The rarity of transitions in the interior ice pack, reinforces the idea that sea ice acts as a stabilizing control on the upper ocean mixing regime . Panel (d) confirms that mixing regimes are persistent across perennial sea ice grid cells, however, there is a non-negligible~~

~~subset, where turbulent forcing is highly variable.~~ (d) indicate that mixing regime instability in the MIZ is governed by transient, event-driven forcing and precedes changes in MIZ extent. This phase offset indicates that regime instability is driven by the rate of ice and surface forcing evolution rather than by MIZ extent itself, with dynamically active transition periods dominating mixing regime variability.

Figure 4 provides ~~further insight into how~~ complementary information into how both local and spatially aggregated values of ~~the La_t vary as a function of SIC, helping to~~ La_t, depend on sea ice concentration (SIC), and helps contextualize the spatial ~~patterns of each mixing regime . The left panel~~ regime structure identified in Figure 3. Panel (a) shows that median ~~La_t values increase monotonically~~ La_t increases with SIC across ~~all spatial scales~~most seasons, indicating a systematic ~~suppression of wave-driven mixing under increasing ice cover . While the lowest La_t values (< 0.43),~~ shift toward shear-dominated conditions as ice cover increases. Conditions associated with strong LT ~~, are found only in open water or sparsely ice-covered conditions, values exceeding 0.94 dominate in areas with~~ potential ($La_t < 0.43$) are largely confined to OW or low SIC, whereas shear-dominated regimes ($La_t > 0.94$) prevail at moderate to high SIC~~, consistent with earlier findings that wave forcing is effectively attenuated by even partial ice coverage~~. This behavior is consistent with the increasing attenuation of wave energy and reduction of Stokes drift under partial ice cover. During summer, however, median La_t exhibits a reduction at high SIC. This deviation is consistent with seasonal changes in ice mechanical properties and surface forcing, under which thinner and more fragmented ice with enhanced floe-scale heterogeneity may permit intermittent penetration of long-period swell into regions that remain nominally ice covered (Ardhuin et al., 2016; Brenner and Horvat, 2024). At the same time, wind stress over melting ice tends to be reduced and spatially variable, which can diminish shear-driven turbulence relative to wave-driven contributions. Within this context, the observed decrease in La_t at high SIC is interpreted as evidence for episodic wave influence under summer ice conditions, indicating that SIC alone does not uniquely constrain the wave impact on upper-ocean turbulence during the melt season. Panel (b) ~~illustrates the pronounced subgrid variability of La_t~~ highlights the local variability of La_t using histograms of the minimum, mean, and maximum values computed over local ~~3×3 grid cell neighborhoods. We defined these neighborhood metrics to provide physical insight into the surrounding~~ 3×3 grid-cell neighborhoods. These neighborhood diagnostics are introduced to characterize the local dynamical environment experienced by each MIZ grid cell. ~~Specifically, $La_t^{\min}$~~ The minimum value, $La_t^{\min}$, identifies the most ~~wave-affected neighboring point , serving as~~ wave-influenced neighboring point and provides an upper bound on local wave ~~influence, while $La_t^{\max}$~~ impact, while $La_t^{\max}$ reflects the most shear-dominated condition in the vicinity. The ~~spatial mean(La_t^{mean}) yields a smoother representation that~~ neighborhood mean, La_t^{mean}, closely tracks the ~~local (single grid cell) La_t, highlighting dominant regime tendencies. In contrast,~~ single-grid-cell La_t, representing the dominant local regime, whereas the extremes reveal ~~localized deviations that are masked by coarser averages. From this interpretation we realize that mixed-forcing regimes in the MIZ are not only seasonally modulated but also sensitive to spatial scale, suggesting a potential need for subgrid-aware approaches in OSBL parameterizations~~ local scale variability that is masked by spatial averaging. Together, these distributions demonstrate that mixing regimes within the MIZ arise not only from seasonal modulation of SIC but also from strong spatial heterogeneity in wave and shear forcing at scales smaller than the model grid. This scale dependence suggests that conventional one-dimensional

upper-ocean boundary layer parameterizations may inadequately represent mixing processes under partial ice cover, motivating the use of regime-based or local scale-aware approaches in ice–ocean models.

2.4 Pan-Arctic dissipation rates and normalized VKE

~~This section highlights the energetic role of LT in the Arctic beyond spatial regime classification. We examine the dissipation rate ε and its enhancement relative to the expected dissipation if only shear-driven mixing were present.~~ Figure ~~5a displays the pan-Arctic mean dissipation rate over the~~ 5 provides energetic context for the regime instability patterns identified in Figures 3–4 by explicitly characterizing both the magnitude and intermittency of mechanically driven upper-ocean dissipation under partial ice cover. Panel (a) shows the spatial distribution of median mechanical dissipation over 2018–2022 ~~period. Elevated ε values are found along the climatological MIZ and in marginal seas, where wave–ice interactions persist seasonally. Dissipation hotspots exceed $\varepsilon \approx 3 \times 10^{-7}\ \mathrm{m^2 s^{-3}}$, aligning with in-situ observations of enhanced turbulent mixing in wave-active polynyas and shelf seas (Rippeth and Fine, 2022).~~

~~Additionally, we compute the normalized dissipation ratio $\varepsilon_{\mathrm{LT}}/\varepsilon_{\mathrm{shear}}$ (figure 5b), which exhibits a strong inverse dependence on the Langmuir number La_t, consistent with theoretical and LES-based scaling relationships (Grant and Belcher, 2009; Li et al., 2019) . Specifically, the theoretical scaling $\varepsilon_{\mathrm{LT}}/\varepsilon_{\mathrm{shear}} \propto 1/La_t^2$, derived from idealized mixed-layer turbulence theory, is included for reference and broadly captures the observed trend. Enhancement ratios exceeding 2 are observed at low La_t (< 0.5) , indicating significant Langmuir-induced mixing. However, the observed enhancement remains below the theoretical limit, reflecting the modulating effects of stratification and sea ice cover. These high ratios primarily occur in low-SIC and OW regions, while compact sea ice strongly suppresses LT contributions. Seasonal histograms of spatially averaged dissipation (Figure 5c)reveal significantly higher values during September compared to March, reflecting both enhanced wave activity and reduced sea ice extent, favoring LT generation. This seasonal amplification is consistent with LES results that show LT strengthening during low-stratification and high-wave periods (?).~~

~~Panels (d) and (e) further quantify the role of Lusing two complementary diagnostics. Figure 5d shows the spatially averaged Langmuir enhancement factor, $\mathcal{E}(\mathcal{L}^{-1}_{8}) - 1$, partitioned by sea ice concentration regime. This metric reflects the potential amplification of turbulence due to wave~~for SIC $\geq$ 0.15. Persistent dissipation is concentrated along the marginal ice zone, wave-exposed shelves, and the seasonal ice edge, while the interior pack ice exhibits weak and spatially uniform dissipation. This pattern reflects the long-term background structure of mechanical energy input and identifies regions where wind–~~wind interactions when Langmuir processes are active. The enhancement is strongest in open water (~ 0.45)~~ wave forcing recurrently couples to the upper ocean. Panel (b) reveals a complementary aspect of the forcing environment by mapping dissipation intermittency, quantified as $log_1 0$ (P90/median). High intermittency is strongly localized to narrow MIZ regions and ice edge corridors, indicating that dissipation in these areas is dominated by episodic, burst-like events rather than sustained forcing. In contrast, regions with elevated median dissipation but low intermittency experience comparatively steady energy input. The close spatial correspondence between highly intermittent dissipation and previously identified regime-transition hotspots demonstrates that frequent mixing-regime changes arise preferentially where competing wind-, ~~moderate in the marginal ice zone (MIZ; ~ 0.15), and negligible under compact sea ice. In contrast, Figure5e presents the time-weighted fractional~~

contribution of Langmuir-induced dissipation to wave-, and ice-mediated processes alternately dominate on short timescales. The Arctic-wide time series in panel (c) further emphasizes the event-driven nature of mechanical dissipation, with variability dominated by intermittent extremes superimposed on a low median background. The large interquartile range relative to the median indicates that rare, high-energy events contribute disproportionately to temporal variability, consistent with the episodic forcing implied by the total dissipation budget. This panel captures the realized impact of LT over the total simulation period by integrating both wind- and wave-driven components across time . Despite low La_t values indicating wave-dominant conditions, the actual dissipation may remain shear-dominated due to intermittent high-wind events or periods when LT is suppressed, such as under partial or full ice cover. intermittency index. Panel (d) shows that this intermittency is seasonally modulated, with dissipation peaking during late summer and early autumn when ice cover is thinning and wave penetration is enhanced, and reaching a minimum during late winter under consolidated ice.

To complement the

2.5 Impact of wind–wave misalignment on Langmuir turbulence efficiency

While Figure 5 demonstrates that mechanically driven dissipation in the MIZ is highly intermittent and dominated by episodic events, the extent to which wave-induced forcing contributes to vertical mixing depends critically on the relative alignment of wind and waves. To isolate the role of wind–wave geometry in modulating Langmuir-driven mixing, we explicitly compare wind-aligned and dynamically projected Langmuir diagnostics using both local time series and pan-Arctic assessment, we analyze the temporal evolution statistics. This analysis distinguishes between the *existence* of Langmuir forcing, as indicated by the turbulent Langmuir number La_t, and the *efficiency* with which that forcing is converted into vertical motions under realistic wind–wave alignment.

Because wind–wave misalignment is a local geometric property of the surface forcing rather than a spatially averaged quantity, all misalignment diagnostics are evaluated at the native model grid scale. Spatial smoothing does not qualitatively alter the inferred suppression of Langmuir-driven mixing vertical motions, but it obscures the episodic nature of misalignment events and is therefore avoided here.

We first illustrate the impact of wind–wave misalignment using time series extracted at two dynamically contrasting sites using 100 km-radius kernel averages centered in the Central Arctic (84.5°N, 202.0°E) and the Barents Sea (78.0°N, 43.9°E) . locations representative of (i) the seasonal MIZ and (ii) the consolidated central Arctic (Figure 6presents the 2022 time series of turbulent dissipation rate (ε)and). For each site, we show the standard La_t, the projected Langmuir number accounting for dynamically oriented Langmuir cells (La_{proj}), the mixed-layer-averaged vertical kinetic energy ($\langle w'^2 \rangle_{H_{\mathrm{ML}}}$), alongside velocity variance $\langle w'^2 \rangle_{H_{\mathrm{ML}}}$ estimated from LES-based scalings, and daily sea ice concentration (SIC). At both locations, LT-enhanced metrics exhibit pronounced seasonal variability, tightly coupled to wave exposure modulated by evolving ice conditionsTogether, these metrics allow direct comparison between the potential for Langmuir forcing and its realized efficiency under evolving wind–wave alignment.

In the Central Arctic, LT-enhanced dissipation rates ($\varepsilon_{\mathrm{LT}}$) closely track the shear-only estimates but consistently exceed them, including during periods of compact At the MIZ site, both La_t and La_{proj} exhibit pronounced seasonal variability

associated with the expansion of the ice cover. ~~Seasonal peaks emerge in January and April-coinciding with intensified wind forcing- and again in October following a mid-summer plateau. This persistent exceedance suggests sustained LT potential even under high SIC, likely due to mobile or loosely packed conditions that permit momentum transfer. Additionally, we observe a peak in dissipation in July, as SIC starts decreasing~~Periods of reduced SIC permit wave penetration and enhanced Stokes drift, leading to episodic transitions into mixed- and wave-driven forcing regimes. During these intervals, La_{proj} is frequently lower than La_t, reflecting geometric suppression of Langmuir forcing due to wind–wave misalignment. These misalignment events coincide with elevated vertical kinetic energy, indicating that Langmuir turbulence is energetically active but operates at reduced efficiency relative to a wind-aligned reference state. In contrast, ~~VKE shows less regular seasonality but exhibits distinct peaks in end of March/April and December that surpass the dissipation rate, implying episodic energy injections. These events likely reflect storm-driven activity under high SIC , where wind and wave forcing remain effective despite partial~~ periods of high SIC are characterized by weak vertical kinetic energy and little distinction between La_t and La_{proj}, consistent with strong wave attenuation beneath the ice cover.

The ~~Barents Sea displays a different evolution, shaped by substantial springtime ice retreat and transition to OW by early summer. This shift is accompanied by sharp increases in VKE during April-May, consistent with enhanced LT potential during early retreat sea ice phases. Throughout~~ central Arctic site exhibits markedly different behavior. Persistently high SIC limits wave penetration throughout most of the year, ~~LT-enhanced dissipation remains elevated above the shear-only baseline, with particularly strong signals in fall and winter. Compared to the Central Arctic, active LT conditions occur earlier and persists longer, facilitated by a deeper climatological mixed layer and generally lower SIC. Interestingly, VKE diminishes as SIC drops toward open-water conditions-a pattern suggesting that LT activity in this marginal setting peaks under intermediate SIC (~0.4–0.7), where wave penetration, ice damping, and~~ resulting in consistently large Langmuir numbers and weak vertical kinetic energy. Differences between La_t and La_{proj} are small and infrequent, indicating that wind–wave ~~alignment optimally enhance vertical energy. This seasonal decline likely reflects increasing upper-ocean stratification due to surface heating and sea ice melt, which suppresses vertical motions despite low sea ice concentration. The disappearance of VKE highlights the sensitivity of Langmuir-driven turbulence to evolving wave conditions and buoyancy structure, consistent with theoretical expectations and LES results (Van Roekel et al., 2012; Li et al., 2019).~~ misalignment plays a secondary role where wave-induced Stokes drift is already strongly suppressed. Even when brief reductions in SIC occur, the associated misalignment produces only modest changes in vertical kinetic energy due to the overall lack of energetic wave forcing.

These local time series demonstrate that ~~LT potential in both regions is strongly modulated by SIC and wave forcing, but not limited to OW conditions. Even under compact ice, enhanced dissipation and elevated VKE imply that wind-wave momentum coupling remains dynamically active. The co-variation of $\varepsilon_{\mathrm{LT}}$ and $\langle w'^2 \rangle_{H_{\mathrm{ML}}}$ confirms that Langmuir processes contribute not only to enhanced dissipation but also to sustained vertical momentum transfer throughout the year. These findings reinforce the spatial patterns identified in Figure 5, highlighting the importance of representing LT variability when modeling upper-ocean mixing in seasonally ice-covered environments~~wind–wave misalignment does not determine whether Langmuir turbulence is present, but rather modulates its efficiency when wave-driven forcing is active. Misalignment effects are therefore most pronounced in the MIZ, where partial ice cover allows wave penetration and energetic Langmuir motions, while they remain

muted in the consolidated central Arctic. This motivates a broader, pan-Arctic assessment of misalignment-driven suppression of Langmuir turbulence efficiency, which we quantify below using a nondimensional efficiency metric.

To quantify the impact of wind–wave misalignment across the Arctic, we define the ratio

$$R_{LT} = \langle w'^2 \rangle_{La_{\mathrm{proj}}} / \langle w'^2 \rangle_{La_t},$$

which measures the efficiency of Langmuir-driven ~~mixing. This ratio compares two formulations of the Langmuir number: one incorporating projection onto the wind direction (La_{proj}) and one assuming perfect alignment (La_t). Both formulations use the same enhancement framework described in Section 2.2.3. Figure 7 visualizes the dissipation ratio $\varepsilon_{La_{\mathrm{proj}}}/\varepsilon_{La_t}$ and quantifies the modulation from misalignment, revealing moderate suppression across the interior ice pack, typically in the 0.7–0.9 range. This suggests that LT remains active but is somewhat diminished due to wind–wave misalignmentunder high sea ice concentration~~vertical motions relative to a wind-aligned reference state. Here, R_{LT} is interpreted as an efficiency factor: values near unity indicate that Langmuir-driven vertical motions approach their wind-aligned maximum, while lower values quantify the fraction of Langmuir potential lost due to wind–wave misalignment.

~~The VKE difference map further supports this interpretation, showing $\Delta\mathrm{VKE} \approx 0$ across much of the central Arctic. This implies that~~ Figure 7a shows that R_{LT} decreases systematically with increasing Langmuir cell orientation angle α_{LOW}, demonstrating a progressive suppression of vertical kinetic energy as wind–wave alignment deteriorates. R_{LT} approaches unity only under near-perfect alignment and does not exceed unity, confirming that Langmuir cell rotation acts as a purely geometric limiter rather than an amplifying mechanism. Across the MIZ, wind–wave misalignment typically reduces Langmuir-induced vertical ~~motions are minimal in these regions, regardless of whether wind–wave misalignment is explicitly accounted for. Rather than directional decorrelation, it is the persistent presence of compact sea ice that primarily suppresses the Stokes drift and surface wave input needed to sustain LT. Consequently, both the standard enhancement factor $\mathcal{E}_{La_t}$ and its misalignment-corrected counterpart $\mathcal{E}_{La_{\mathrm{proj}}}$ yield similarly low estimates of vertical kinetic energy in these regimes. This highlights that dense sea ice—not misalignment—is the dominant limiting factor for LT activity in the central Arctic~~velocity variance by 30–50% relative to wind-aligned estimates, with stronger suppression during shear-dominated conditions. Recasting the same relationship in terms of $\cos^2(\alpha_{\mathrm{LOW}})$ reveals a near-collapse of R_{LT} across shear-dominated, mixed-forcing, and wave-dominated regimes (Figure 7b). In all regimes, Langmuir efficiency closely follows the ideal geometric scaling $R_{LT} = \cos^2\alpha$, with regime-dependent offsets reflecting differences in baseline forcing rather than changes in functional behavior. This collapse demonstrates that wind–wave alignment primarily controls the *efficiency* with which Langmuir forcing is converted into vertical motions, while the underlying forcing regime governs the available Langmuir potential.

~~In particular, the dissipation formulation includes an explicit $|\cos(\theta_{\mathrm{ww}})|$ scaling term in addition to the projected Langmuir number, whereas for the VKE expression, the angle dependence is absorbed into the scaling via La_{proj}.As a result, VKE differences are more spatially uniform and weaker than the mapped dissipation ratio. This structural distinction between dissipation and VKE parameterizations likely contributes to the stronger regional variability observed in dissipation ratios compared to VKE. In panel (c) , the binned relationship between dissipation ratio and $\cos(\theta_{\mathrm{ww}})$ reveals a near-linear dependence. As alignment improves ($\cos(\theta_{\mathrm{ww}}) \to 1$), the dissipation ratio approaches unity, while strong misalignment ($\cos(\theta_{\mathrm{ww}}) < 0.6$)~~

results in up to 50% suppression of wave-enhanced dissipation. Colored by SIC, the scatterplot confirms that misalignment effects are most pronounced in partially ice-covered waters, where directional variability is high and LT remains activeAcross all MIZ grid cells ($0.15 \leq \mathrm{SIC} \leq 0.8$), the median value of R_{LT} is 0.84, with an interquartile range of 0.34–1.00, indicating that wind–wave misalignment generally produces modest suppression of Langmuir-driven vertical velocity variance, while occasionally reducing it by more than 60% during strongly misaligned events. The full distribution of R_{LT} across the MIZ is shown in Supplemental Fig. S3. Wind–wave misalignment therefore emerges as a physically robust, regime-independent modulator of Langmuir turbulence efficiency in the Arctic, distinct from variations in the local wave–shear balance.

Interestingly, the MIZ exhibits only modest differences between La_t- and La_{proj}-based dissipation estimates, with mean dissipation ratios around 0.8. This relatively weak sensitivity to misalignment in the MIZ may arise from several factors. First, both wind and wave fields in the MIZ are typically more energetic and spatially coherent than in the interior ice pack, reducing the likelihood of extreme directional decoupling (Stopa et al., 2018). Second, local wave–wind climatologies in the MIZ may already reflect partial alignment due to fetch-limited wave growth under intermediate ice concentrations. Third, under strong turbulence forcing , the nonlinear response of Langmuir enhancement factors to La_t or La_{proj} may saturate, such that moderate misalignment produces only limited suppression. Hence, these factors suggest that in the MIZ , projected Stokes–wind alignment (as captured in La_{proj}) introduces only a secondary correction to La_t-based dissipationestimates, supporting the use of simpler diagnostics for bulk assessments while highlighting the added value of alignment-aware metrics in regional and dynamic ice-covered regimes.

Sensitivity of Langmuir-driven dissipation and VKE to wave–wind misalignment. (a) Spatial distribution of dissipation ratio $\epsilon_{\mathrm{La_{proj}}}/\epsilon_{\mathrm{La_t}}$, quantifying the suppression of dissipation due to misalignment. (b) VKE difference ($\Delta\mathrm{VKE} = \mathrm{VKE}_{\mathrm{La_{proj}}} - \mathrm{VKE}_{\mathrm{La_t}}$), highlighting negative anomalies across the ice pack. (c) Dissipation ratio as a function of directional alignment ($\cos(\theta_{\mathrm{WW}})$), with point color indicating local SIC. Shaded band shows $\pm 1\sigma$ about the mean in each bin.

3 Discusion and Conclusions

3 Discussion and Conclusions

Our results provide a comprehensive assessment of the spatiotemporal variability of Langmuir turbulence (LT)

3.1 The marginal ice zone as a dynamically distinct mixing regime

Our results demonstrate that surface forcing capable of sustaining Langmuir turbulence (LT) in the Arctic is both spatially confined and temporally intermittent. Conditions resembling open-water wind–wave forcing occur predominantly within the seasonal marginal ice zone (MIZ), while the interior pack ice remains largely shear dominated. Even within the MIZ, joint exceedance of wind stress and Stokes drift rarely exceeds 20% of the time, indicating that LT beneath ice is not a persistent background process but instead emerges episodically.

A pronounced seasonal asymmetry further characterizes this behavior. Despite the largest spatial extent of the MIZ during summer, LT-relevant forcing and Langmuir enhancement are weakest in this season. This counterintuitive result reflects the competing effects of ice retreat and wave attenuation: moderate ice concentrations efficiently damp Stokes drift, consistent with theoretical and observational studies documenting rapid decay of wave energy and Stokes transport under partial ice cover (Liu and Mollo-Christensen, 1988; Ardhuin et al., 2016; Herman, 2017), while summer winds tend to be weaker and less coherent. As a result, expanded MIZ area does not translate into enhanced LT activity.

In contrast, winter and transitional seasons exhibit more frequent and spatially coherent open-water–like forcing along the evolving ice edge. During these periods, episodic storms generate strong winds and long-period swell that can temporarily overcome wave attenuation and penetrate into the MIZ (Thomson, 2022; Boutin et al., 2022). These events produce brief but dynamically significant excursions toward low La_t, enhanced mechanical dissipation, and elevated LT efficiency. Taken together, our results show that the seasonal imprint of LT in the Arctic ~~Ocean, revealing that LT is dynamically modulated by the interplay between wind stress, wave accessibility, and sea ice cover. Rather than existing as distinct binary states of wave- or shear-dominance, Arctic upper-ocean turbulence frequently manifests as a mixed-forcing regime, particularly in the MIZ , where both mechanisms co-occur with varying intensities. Elevated surface shear stress across the MIZ and into the interior pack indicates that wind forcing alone is frequently sufficient to support LT, provided wave conditions permit. However, Stokes drift penetration, governed by~~ is governed by the intensity and coherence of wind–wave forcing rather than by MIZ extent alone. This finding is consistent with conceptual views of the MIZ as a dynamically active wave–ice interaction zone rather than a purely geometric transition region (Squire and Williams, 2008; Horvat and Tziperman, 2015).

3.2 Sea ice regulation of Stokes drift and Langmuir turbulence potential

Across all diagnostics, sea ice concentration (SIC) ~~, modulates the degree to which wave-driven turbulencecan be realized. This asymmetry yields a regime where wind-driven shear is often present, but wave forcing is spatially and temporally constrained, creating conditionsfavorable for intermittent but energetically significant LT events~~emerges as a first-order regulator of the *mean* balance between wave- and shear-driven turbulence. For most seasons, median La_t increases monotonically with SIC, reflecting progressive suppression of Stokes drift relative to wind stress as ice cover increases. Consequently, the central Arctic is characterized by persistently shear-dominated conditions, long regime persistence, and weak variability in LT-related metrics.

~~The seasonal expansion of LT-favorable zones during late summerand early fall coincides with enhanced wave exposure and reduced SIC, producing stronger LT signals during these periods. Spring and winter medians, by contrast, reveal sharply bounded~~ Departures from this monotonic relationship during summer, most notably reduced La_t ~~transitions that reflect suppression under compact ice . These are most pronounced in the MIZ, where SIC and wave energy vary over short distances, leading to rapid shifts in mixing regime. Our classification framework confirms that pure wave-dominant conditions are rare; instead, mixed-forcing regimes dominate across the MIZ. These emerge under partial ice cover, moderate SIC, and episodic wave events, suggesting that~~ at higher SIC, do not indicate sustained wave forcing within the interior pack. Instead, they reflect intermittent wave penetration enabled by thinner, more fragmented ice and enhanced floe-scale heterogeneity during the

melt season. Under these conditions, long-period swell can episodically access regions that remain nominally ice covered, temporarily reducing La_t without establishing a persistent wave-driven regime. These results highlight that while SIC controls the background forcing state, the ~~MIZ functions as a responsive and sensitive transition zone between open-water and ice-covered states.~~ mechanical properties of the ice and the spectral characteristics of the wave field modulate the realization of wave influence in ways not captured by concentration alone.

~~Scale-based diagnostics diagnostics reinforce this interpretation. Histogram-based kernel analyses of La_t reveal that while gridcell means suggest shear dominance, neighboring extremes often reach wave-favorable values ($La_t^{\min} < 0.43$), indicating that turbulence regimesare highly heterogeneous at the subgrid scale. Such variability, driven by SIC and directional wave fields can induce intense but spatially confined LT activity, particularly in the MIZ . These results highlight a key limitation of coarse-resolution (25 km) models, where grid-mean diagnostics may obscure critical small-scale variability in surface forcing that modulates mixing regime dynamics.~~

3.3 Forcing intermittency, regime instability, and Langmuir efficiency

~~Dissipation and vertical kinetic energy (VKE) estimates further substantiate these findings. Langmuir-enhanced dissipation is elevated in the~~ The regime-based analysis further reveals that the MIZ is not merely a spatial transition zone but a dynamically distinct environment characterized by enhanced variability and frequent reorganization of surface forcing. Regime instability peaks when grid cells reside near thresholds separating shear-, mixed-, and ~~open-water sectors, with peak values exceeding $\epsilon \sim 3 \times 10^{-7}$ m^{2}s^{-3}, consistent with prior observations in wave-active polynyas and marginal seas. In the Central Arctic, however, dissipation is generally lower and more seasonally muted, although transient increases in VKE and ϵ coincide with brief periods of moderate SIC. These results suggest that LT in compact ice is limited but not negligible, potentially driven by residual swell energy or directional wave refraction.~~ wave-dominated regimes, rather than when the MIZ is most extensive. Periods of broad MIZ coverage are often dynamically stable, whereas narrow, rapidly evolving ice edges promote frequent regime switching. This behavior extends earlier work showing that ice-edge variability is governed by dynamical thresholds rather than ice extent alone (Horvat et al., 2016).

~~We also examined the influence of wind–wave misalignment on LT diagnostics using the projected Langmuir number La_{proj}. Arctic-wide maps show that incorporating misalignment reduces LT-driven dissipation and VKE in the central basin, with suppressions exceeding 40% in some areas. However, in the MIZ, the impact of misalignment was notably modest, with dissipation ratios ($\varepsilon_{La_{\mathrm{proj}}}/\varepsilon_{La_t}$) close to 0.8–0.9, and minimal VKE reductions. This suggests that in dynamic, partially~~ Energetic diagnostics indicate that this instability is driven primarily by the intermittency of mechanical dissipation rather than by its mean magnitude. Highly intermittent dissipation is strongly localized to the same MIZ corridors that exhibit frequent regime transitions, demonstrating that episodic forcing events associated with storms and wave penetration dominate the dynamical evolution of the system. This finding aligns with broader evidence that turbulent mixing in both open-ocean and ice-covered ~~environments where waves and winds are both active, the alignment angle may already be implicitly constrained by regional climatologies, or that the absolute magnitude of forcing dominates the response. This result supports the use of La_t for diagnosing broad regional patterns, while highlighting the added value of alignment-aware metrics in regional,~~

more dynamic regions. environments is controlled by intermittent, high-energy events rather than by time-mean forcing (Belcher et al., 2012; McWilliams, 2016; Ardhuin et al., 2016; Thomson, 2022; Boutin et al., 2022).

Concluding Explicitly accounting for wind–wave misalignment further refines the diagnosis of Langmuir-driven mixing. Comparisons between wind-aligned and dynamically projected Langmuir diagnostics show that misalignment acts as a systematic geometric constraint on LT efficiency by reducing the effective Stokes shear projected onto the Langmuir cell axis. This behavior is consistent with theoretical and large-eddy simulation studies demonstrating that Langmuir turbulence intensity depends not only on the magnitude of Stokes drift but also on its orientation relative to the wind stress (McWilliams et al., 1997; Harcourt an . Increasing misalignment suppresses vertical velocity variance even when wave forcing is present.

In our analysis, wind–wave misalignment reduces the realized contribution of LT to vertical mixing across all surface forcing regimes without altering the underlying regime classification. Thus, while La_t determines whether Langmuir forcing is present, geometric alignment governs how efficiently that forcing is converted into vertical motions. Together, our results show demonstrate that LT in the Arctic varies is highly heterogeneous in space and time, responding dynamically to changes variations in waves, sea ice, and wind geometry. The MIZ emerges as the most sensitive zone for transitions between mixing regimes. While standard Langmuir number diagnostics capture broad patterns, they tend to overestimate turbulence under compact ice and underestimate it in the MIZ, where mixed forcingdominates. Incorporating wind–wave misalignment improves realism but adds only a modest correction in the MIZ. As Arctic sea ice continues to thin and retreat, LT and mixed-forcing conditions are likely to expand, underlining primary region where intermittent forcing, geometric constraints, and competing production mechanisms interact, underscoring the need for regime-aware turbulence parameterizations to simulate and geometry-aware representations of upper-ocean structure and air–ice–ocean feedbacks under climate changemixing under partial ice cover.

3.4 Limitations and Future Directions

Our approach is based on bulk diagnostics and empirical scalings , and thus carries several empirically derived scalings and therefore carries several important limitations. The use of ∼25 km resolution fields limits our ability to resolve fine-scale processes such as mesoscale and submesoscale eddies, floe-scale wave attenuation, and narrow leads and polynyas, all of which modulate LT can locally modulate Langmuir turbulence and upper-ocean mixing. Although local kernel statistics help capture some subgrid variability, direct evaluation neighborhood-based statistics partially capture local heterogeneity, direct assessment of small-scale LT dynamics requires high-resolution modeling and in situ observations. AdditionallyLangmuir dynamics ultimately requires higher-resolution modeling and targeted *in situ* observations.

In addition, our analysis uses relies on a coupled sea ice-wave simulation where mixed-layer depth is not dynamically responsive to wind–wave forcing , without ice–wave framework in which the ocean mixed layer does not respond dynamically to wind–wave forcing and explicit ocean stratification or feedbacks . This constrains the accuracy of vertical mixing diagnostics and highlights the need for fully coupled ocean–ice –wave modelsto more realistically simulate LT evolution in the Arctic. feedbacks are not resolved. Mixed-layer depth and buoyancy effects are therefore prescribed rather than prognostic, constraining the realism of the diagnosed vertical mixing response. In particular, buoyancy-driven convection and Langmuir turbulence are expected to interact nonlinearly in ice-covered and meltwater-influenced environments, yet their relative contributions remain

poorly constrained in the present framework. As a result, the diagnostics presented here should be interpreted as indicators of Langmuir *potential* rather than as predictions of realized turbulent states.

~~Future work should focus on integrating directional wave spectra and wind–wave coupling from fully coupled ocean–wave–icemodels, allowing for a more explicit treatment of misalignment effects and wave propagation under ice. Observational efforts~~

3.4.1 Implications for ocean and climate modeling.

Despite these limitations, our results provide several clear implications for the representation of upper-ocean mixing under partial ice cover in climate and Earth system models. First, the strong intermittency and regime dependence of Langmuir turbulence in the MIZ imply that parameterizations based on time-mean forcing or sea ice concentration alone are unlikely to capture the episodic nature of mechanically driven mixing. Instead, regime-aware formulations that respond to joint wind–wave conditions and their temporal variability are required.

Second, our analysis demonstrates that wind–wave misalignment acts as a systematic geometric limiter on LT efficiency, independent of the underlying wave–shear balance. This finding suggests that existing Langmuir parameterizations, which often assume wind-aligned Stokes drift, may systematically overestimate vertical mixing in partially ice-covered regions unless geometric effects are explicitly accounted for. Incorporating misalignment-aware scaling factors or projected Stokes drift formulations offers a physically grounded pathway for improving LT representations without substantially increasing model complexity.

Finally, the spatial confinement of LT-relevant forcing to narrow, evolving MIZ corridors highlights the need for parameterizations that are robust across sharp transitions in surface state. In coarse-resolution models, where the MIZ is often poorly resolved, neglecting this spatial and temporal localization may lead to either excessive mixing within the interior pack or insufficient mixing near the ice edge. Our results therefore motivate the development of scale-aware and regime-based mixing schemes that adapt dynamically to ice concentration, wave exposure, and wind–wave geometry.

Addressing these challenges ultimately requires fully coupled ocean–wave–ice models that resolve stratification, wave propagation beneath ice, ~~including coordinated field campaigns using~~ and wind–wave misalignment simultaneously. Recent and ongoing studies are beginning to resolve Langmuir turbulence under partially ice-covered and weakly stratified regimes using large-eddy simulations, regional modeling, and coordinated observations (e.g., Brenner et al., 2023; Lee et al., 2025). These efforts provide a clear pathway toward stratification-aware, ice-modified Langmuir parameterizations.

Complementary observational efforts are also essential. Coordinated field campaigns employing autonomous profilers, SWIFT drifters, and satellite altimetry ~~, are also critical for validating LT~~ will be critical for evaluating Langmuir diagnostics and parameterizations in ice-covered waters. In particular, ~~future~~ observational and modeling studies should prioritize the MIZ, where ~~our results suggest that mixed forcing dominates and where wave–ice–wind~~ wave–ice–wind interactions are most dynamically active. Finally, ~~evaluating~~ quantifying the impact of ~~LT~~ Langmuir turbulence on vertical tracer transport, stratification erosion, and ~~ice–ocean heat exchange within~~ ice–ocean heat exchange in climate models will be essential ~~to fully quantify the role of LT~~ for assessing its broader role in the evolving Arctic system.

~~Definitions and descriptions of available parameters from neXtSIM and WW3 models.~~ **Parameter Description Units** ~~τ_x Eastward stress at ocean surface Pa τ_y Northward stress at ocean surface Pa u_{ice} Sea ice x velocity $\mathrm{m\,s^{-1}}$ v_{ice} Sea ice y velocity $\mathrm{m\,s^{-1}}$ SIC Sea ice concentration - SIC_{young} Young ice concentration - SIT_{young} Young ice thickness m SIT Sea ice thickness m SNT Surface snow thickness m D_{max} Maximum floe size m D_{mean} Mean floe size m SSS Sea surface salinity PSU SST Sea surface temperature $^\circ$C $T_{2\text{m}}$ 2-m air temperature $^\circ$C dir Sea surface wave from direction degrees d_p Sea surface wave peak direction degrees f_p Sea surface wave peak frequency Hz H_s Significant wave height m $ic1$ Ice thickness m $ic3$ Average ice floe diameter m ice Sea ice area fraction - t_{02} Mean wave period (from second moment) s tus Northward Stokes transport - us Northward surface Stokes drift - wnd wind speed $\mathrm{m\,s^{-1}}$~~

Seasonal bar plots of high Stokes drift velocities ($u_{s(0)}$) and surface friction velocities (u_*) in the MIZ.

. The model outputs and post-processed Langmuir turbulence diagnostics used in this study are publicly available via Zenodo at https://zenodo.org/records/17372007. Analysis scripts are hosted on GitHub at https://github.com/atavri/Langmuir_turbulence_Arctic.git. ERA5 atmospheric reanalysis data are available from the Copernicus Climate Data Store, and the GLORYS12V1 ocean reanalysis is available through the Copernicus Marine Service.

. A.T. led the study, including conceptualization, analysis, and writing of the original draft. C.H., B.P., and A.T. contributed to interpretation of results and manuscript review and editing. G.B. contributed to model data curation and technical support. A.H. and A.K. contributed to early analysis and scientific discussion.

. The authors declare that they have no competing interests.

. This research was supported in part by the National Science Foundation (NSF OPP-2146910 and OCE-2148655) and by Schmidt Sciences, LLC through the SASIP project. The simulations were performed ~~on~~ using resources provided by ~~Sigma2 - the~~ Sigma2—the National Infrastructure for High-Performance Computing and Data Storage in Norway.

We thank Sam Brenner for their assistance during the project initialization phase and for insightful discussions that helped shape the use of the Langmuir turbulence parameterizations.

References

Ali, A., Christensen, K. H., Breivik, Ø., Malila, M., Raj, R. P., Bertino, L., Chassignet, E. P., and Bakhoday-Paskyabi, M.: A comparison of Langmuir turbulence parameterizations and key wave effects in a numerical model of the North Atlantic and Arctic Oceans, Ocean Modelling, 137, 76–97, 2019.

Ardhuin, F., Sutherland, P., Doble, M., and Wadhams, P.: Ocean waves across the Arctic: Attenuation due to dissipation dominates over scattering for periods longer than 19 s, Geophysical Research Letters, 43, 5775–5783, 2016.

Ardhuin, F., Boutin, G., Stopa, J., Girard-Ardhuin, F., Melsheimer, C., Thomson, J., Kohout, A., Doble, M., and Wadhams, P.: Wave attenuation through an Arctic marginal ice zone on 12 October 2015: 2. Numerical modeling of waves and associated ice breakup, Journal of Geophysical Research: Oceans, 123, 5652–5668, 2018.

Ardhuin, F., Otero, M., Merrifield, S., Grouazel, A., and Terrill, E.: Ice breakup controls dissipation of wind waves across southern ocean sea ice, Geophysical Research Letters, 47, e2020GL087 699, 2020.

Armitage, T. W., Bacon, S., Ridout, A. L., Petty, A. A., Wolbach, S., and Tsamados, M.: Arctic Ocean surface geostrophic circulation 2003–2014, The Cryosphere, 11, 1767–1780, 2017.

Belcher, S. E., Grant, A. L., Hanley, K. E., Fox-Kemper, B., Van Roekel, L., Sullivan, P. P., Large, W. G., Brown, A., Hines, A., Calvert, D., et al.: A global perspective on Langmuir turbulence in the ocean surface boundary layer, Geophysical Research Letters, 39, 2012.

Boutin, G., Ardhuin, F., Dumont, D., Sévigny, C., Girard-Ardhuin, F., and Accensi, M.: Floe size effect on wave-ice interactions: Possible effects, implementation in wave model, and evaluation, Journal of Geophysical Research: Oceans, 123, 4779–4805, 2018.

Boutin, G., Lique, C., Ardhuin, F., Rousset, C., Talandier, C., Accensi, M., and Girard-Ardhuin, F.: Towards a coupled model to investigate wave–sea ice interactions in the Arctic marginal ice zone, The Cryosphere, 14, 709–735, 2020.

Boutin, G., Williams, T., Rampal, P., Olason, E., and Lique, C.: Wave–sea-ice interactions in a brittle rheological framework, Cryosphere, 15, 431–457, 2021.

Boutin, G., Williams, T., Horvat, C., and Brodeau, L.: Modelling the Arctic wave-affected marginal ice zone: a comparison with ICESat-2 observations, Philosophical Transactions of the Royal Society A, 380, 20210 262, 2022.

Brenner, S. and Horvat, C.: Scaling simulations of local wind-waves amid sea ice floes, Journal of Geophysical Research: Oceans, 129, e2024JC021 629, 2024.

Brenner, S., Rainville, L., Thomson, J., Cole, S., and Lee, C.: Comparing observations and parameterizations of ice-ocean drag through an annual cycle across the Beaufort Sea, Journal of Geophysical Research: Oceans, 126, e2020JC016 977, 2021.

Brenner, S., Horvat, C., Hall, P., Lo Piccolo, A., Fox-Kemper, B., Labbé, S., and Dansereau, V.: Scale-dependent air-sea exchange in the polar oceans: Floe-floe and floe-flow coupling in the generation of ice-ocean boundary layer turbulence, Geophysical Research Letters, 50, e2023GL105 703, 2023.

Collins, C., Doble, M., Lund, B., and Smith, M.: Observations of surface wave dispersion in the marginal ice zone, Journal of Geophysical Research: Oceans, 123, 3336–3354, 2018.

Cooper, V. T., Roach, L., Thomson, J., Brenner, S., Smith, M., Meylan, M., and Bitz, C.: Wind waves in sea ice of the western Arctic and a global coupled wave-ice model, Philosophical Transactions of the Royal Society A, 380, 20210 258, 2022.

Copernicus Marine Service: Global Ocean Reanalysis Products (GLORYS12V1), https://doi.org/10.48670/moi-00021, gLOBAL_REANALYSIS_PHY_001_030, accessed [July 2025], 2020.

Craik, A. D. and Leibovich, S.: A rational model for Langmuir circulations, Journal of Fluid Mechanics, 73, 401–426, 1976.

D'Asaro, E. A.: Turbulence in the upper-ocean mixed layer, Annual review of marine science, 6, 101–115, 2014.

Dethleff, D. and Kempema, E.: Langmuir circulation driving sediment entrainment into newly formed ice: Tank experiment results with application to nature (Lake Hattie, United States; Kara Sea, Siberia), Journal of Geophysical Research: Oceans, 112, 2007.

Dosser, H. V. and Rainville, L.: Dynamics of the changing near-inertial internal wave field in the Arctic Ocean, Journal of Physical Oceanography, 46, 395–415, 2016.

Drucker, R., Martin, S., and Moritz, R.: Observations of ice thickness and frazil ice in the St. Lawrence Island polynya from satellite imagery, upward looking sonar, and salinity/temperature moorings, Journal of Geophysical Research: Oceans, 108, 2003.

Gargett, A. and Grosch, C.: Turbulence process domination under the combined forcings of wind stress, the Langmuir vortex force, and surface cooling, Journal of Physical Oceanography, 44, 44–67, 2014.

Grant, A. L. and Belcher, S. E.: Characteristics of Langmuir turbulence in the ocean mixed layer, Journal of Physical Oceanography, 39, 1871–1887, 2009.

Harcourt, R. R.: An improved second-moment closure model of Langmuir turbulence, Journal of Physical Oceanography, 45, 84–103, 2015.

Harcourt, R. R. and D'Asaro, E. A.: Large-eddy simulation of Langmuir turbulence in pure wind seas, Journal of Physical Oceanography, 38, 1542–1562, 2008.

Herman, A.: Wave-induced stress and breaking of sea ice in a coupled hydrodynamic discrete-element wave–ice model, The Cryosphere, 11, 2711–2725, 2017.

Hersbach, H., Bell, B., Berrisford, P., Hirahara, S., Horányi, A., Muñoz-Sabater, J., Nicolas, J., Peubey, C., Radu, R., Schepers, D., et al.: The ERA5 global reanalysis, Quarterly journal of the royal meteorological society, 146, 1999–2049, 2020.

Horvat, C. and Tziperman, E.: A prognostic model of the sea-ice floe size and thickness distribution, The Cryosphere, 9, 2119–2134, 2015.

Horvat, C., Tziperman, E., and Campin, J.-M.: Interaction of sea ice floe size, ocean eddies, and sea ice melting, Geophysical Research Letters, 43, 8083–8090, 2016.

Horvat, C., Blanchard-Wrigglesworth, E., and Petty, A.: Observing waves in sea ice with ICESat-2, Geophysical Research Letters, 47, e2020GL087 629, 2020.

Kirillov, S. A., Dmitrenko, I. A., Hölemann, J. A., Kassens, H., and Bloshkina, E.: The penetrative mixing in the Laptev Sea coastal polynya pycnocline layer, Continental Shelf Research, 63, 34–42, 2013.

Kukulka, T., Plueddemann, A. J., Trowbridge, J. H., and Sullivan, P. P.: Rapid mixed layer deepening by the combination of Langmuir and shear instabilities: A case study, Journal of Physical Oceanography, 40, 2381–2400, 2010.

Kukulka, T., Plueddemann, A. J., and Sullivan, P. P.: Inhibited upper ocean restratification in nonequilibrium swell conditions, Geophysical Research Letters, 40, 3672–3676, 2013.

Lee, A., Hutchings, J., Horvat, C., Tavri, A., and Pearson, B.: Impact of Surface Waves on Mixing and Circulation in a Summertime Lead, EGUsphere, 2025, 1–33, 2025.

Leibovich, S.: The form and dynamics of Langmuir circulations, Annual review of fluid mechanics, 15, 391–427, 1983.

Li, Q. and Fox-Kemper, B.: Assessing the effects of Langmuir turbulence on the entrainment buoyancy flux in the ocean surface boundary layer, Journal of Physical Oceanography, 47, 2863–2886, 2017.

Li, Q., Webb, A., Fox-Kemper, B., Craig, A., Danabasoglu, G., Large, W. G., and Vertenstein, M.: Langmuir mixing effects on global climate: WAVEWATCH III in CESM, Ocean Modelling, 103, 145–160, 2016.

Li, Q., Fox-Kemper, B., Breivik, Ø., and Webb, A.: Statistical models of global Langmuir mixing, Ocean Modelling, 113, 95–114, 2017.

Li, Q., Reichl, B. G., Fox-Kemper, B., Adcroft, A. J., Belcher, S. E., Danabasoglu, G., Grant, A. L., Griffies, S. M., Hallberg, R., Hara, T., et al.: Comparing ocean surface boundary vertical mixing schemes including Langmuir turbulence, Journal of Advances in Modeling Earth Systems, 11, 3545–3592, 2019.

Liu, A. K. and Mollo-Christensen, E.: Wave propagation in a solid ice pack, Journal of physical oceanography, 18, 1702–1712, 1988.

Lo Piccolo, A., Horvat, C., and Fox-Kemper, B.: Energetics and Transfer of Submesoscale Brine-Driven Eddies at a Sea Ice Edge, Journal of Physical Oceanography, 54, 1489–1501, 2024.

Longuet-Higgins, M. S. and Stewart, R.: Radiation stress and mass transport in gravity waves, with application to 'surf beats', Journal of Fluid Mechanics, 13, 481–504, 1962.

Manucharyan, G. E. and Thompson, A. F.: Submesoscale sea ice-ocean interactions in marginal ice zones, Journal of Geophysical Research: Oceans, 122, 9455–9475, 2017.

Martin, T., Steele, M., and Zhang, J.: Seasonality and long-term trend of Arctic Ocean surface stress in a model, Journal of Geophysical Research: Oceans, 119, 1723–1738, 2014.

Martin, T., Tsamados, M., Schroeder, D., and Feltham, D. L.: The impact of variable sea ice roughness on changes in A rctic O cean surface stress: A model study, Journal of Geophysical Research: Oceans, 121, 1931–1952, 2016.

McWilliams, J. C.: Submesoscale currents in the ocean, Proceedings of the Royal Society A: Mathematical, Physical and Engineering Sciences, 472, 20160 117, 2016.

McWilliams, J. C. and Sullivan, P. P.: Vertical mixing by Langmuir circulations, Spill Science & Technology Bulletin, 6, 225–237, 2000.

McWilliams, J. C., Sullivan, P. P., and Moeng, C.-H.: Langmuir turbulence in the ocean, Journal of Fluid Mechanics, 334, 1–30, 1997.

Morison, J. H., Long, C. E., and Levine, M. D.: Internal wave dissipation under sea ice, Journal of Geophysical Research: Oceans, 90, 11 959–11 966, 1985.

Muilwijk, M., Hattermann, T., Martin, T., and Granskog, M. A.: Future sea ice weakening amplifies wind-driven trends in surface stress and Arctic Ocean spin-up, Nature Communications, 15, 6889, 2024.

Ólason, E., Boutin, G., Williams, T., Korosov, A., Regan, H., Rheinlænder, J., Rampal, P., Flocco, D., Samaké, A., Davy, R., et al.: The next generation sea-ice model neXtSIM, version 2, EGUsphere, 2025, 1–33, 2025.

Pearson, B. C., Grant, A. L., Polton, J. A., and Belcher, S. E.: Langmuir turbulence and surface heating in the ocean surface boundary layer, Journal of Physical Oceanography, 45, 2897–2911, 2015.

Pinkel, R.: Near-inertial wave propagation in the western Arctic, Journal of physical oceanography, 35, 645–665, 2005.

Polton, J. A. and Belcher, S. E.: Langmuir turbulence and deeply penetrating jets in an unstratified mixed layer, Journal of Geophysical Research: Oceans, 112, 2007.

Rainville, L., Lee, C. M., and Woodgate, R. A.: Impact of wind-driven mixing in the Arctic Ocean, Oceanography, 24, 136–145, 2011.

Rampal, P., Bouillon, S., Ólason, E., and Morlighem, M.: neXtSIM: a new Lagrangian sea ice model, The Cryosphere, 10, 1055–1073, 2016.

Rippeth, T. P. and Fine, E. C.: Turbulent mixing in a changing Arctic Ocean, Oceanography, 35, 66–75, 2022.

Skyllingstad, E. D. and Denbo, D. W.: An ocean large-eddy simulation of Langmuir circulations and convection in the surface mixed layer, Journal of Geophysical Research: Oceans, 100, 8501–8522, 1995.

Skyllingstad, E. D. and Denbo, D. W.: Turbulence beneath sea ice and leads: A coupled sea ice/large-eddy simulation study, Journal of Geophysical Research: Oceans, 106, 2477–2497, 2001.

Smyth, W. D., Skyllingstad, E. D., Crawford, G. B., and Wijesekera, H.: Nonlocal fluxes and Stokes drift effects in the K-profile parameterization, Ocean Dynamics, 52, 104–115, 2002.

Squire, V. and Williams, T.: Wave propagation across sea-ice thickness changes, Ocean Modelling, 21, 1–11, 2008.

Squire, V. A.: A fresh look at how ocean waves and sea ice interact, Philosophical Transactions of the Royal Society A: Mathematical, Physical and Engineering Sciences, 376, 20170 342, 2018.

Stopa, J., Ardhuin, F., Thomson, J., Smith, M. M., Kohout, A., Doble, M., and Wadhams, P.: Wave attenuation through an Arctic marginal ice zone on 12 October 2015: 1. Measurement of wave spectra and ice features from Sentinel 1A, Journal of Geophysical Research: Oceans, 123, 3619–3634, 2018.

Stopa, J. E., Ardhuin, F., and Girard-Ardhuin, F.: Wave climate in the Arctic 1992–2014: Seasonality and trends, The Cryosphere, 10, 1605–1629, 2016.

Sullivan, P. P., McWILLIAMS, J. C., and Melville, W. K.: Surface gravity wave effects in the oceanic boundary layer: Large-eddy simulation with vortex force and stochastic breakers, Journal of Fluid Mechanics, 593, 405–452, 2007.

Thomson, J.: Wave propagation in the marginal ice zone: connections and feedback mechanisms within the air–ice–ocean system, Philosophical Transactions of the Royal Society A, 380, 20210 251, 2022.

Thomson, J. and Rogers, W. E.: Swell and sea in the emerging Arctic Ocean, Geophysical Research Letters, 41, 3136–3140, 2014.

Thomson, J., Ackley, S., Girard-Ardhuin, F., Ardhuin, F., Babanin, A., Boutin, G., Brozena, J., Cheng, S., Collins, C., Doble, M., et al.: Overview of the arctic sea state and boundary layer physics program, Journal of Geophysical Research: Oceans, 123, 8674–8687, 2018.

Tolman, H. L. et al.: User manual and system documentation of WAVEWATCH III TM version 3.14, Technical note, MMAB contribution, 276, 2009.

Van Roekel, L., Fox-Kemper, B., Sullivan, P., Hamlington, P., and Haney, S.: The form and orientation of Langmuir cells for misaligned winds and waves, Journal of Geophysical Research: Oceans, 117, 2012.

Voermans, J., Babanin, A., Thomson, J., Smith, M., and Shen, H.: Wave attenuation by sea ice turbulence, Geophysical Research Letters, 46, 6796–6803, 2019.

Webb, A. and Fox-Kemper, B.: Wave spectral moments and Stokes drift estimation, Ocean modelling, 40, 273–288, 2011.

Yang, D., Chamecki, M., and Meneveau, C.: Inhibition of oil plume dilution in Langmuir ocean circulation, Geophysical Research Letters, 41, 1632–1638, 2014.

~~**Spatial and temporal characteristics of upper ocean mixing regimes in the Arctic.** Panel (a): Dominant mixing regime at each grid cell over 2018–2022, defined as the regime with at least 10% persistence during ice-covered periods (SIC ≥ 0.15). Panel (b): Temporal evolution of mixing regime fractions across all ice-covered grid cells, showing strong seasonal cycles in shear-driven (gold), mixed-forcing (red), and wave-driven (teal) conditions. Black dashed line indicates mean sea ice concentration. Panel (c): Spatial distribution of the normalized frequency of mixing regime transitions, computed as transitions per sea ice-covered day and panel (d): Histogram of normalized transition rates across grid cells with SIC ≥ 0.15.~~

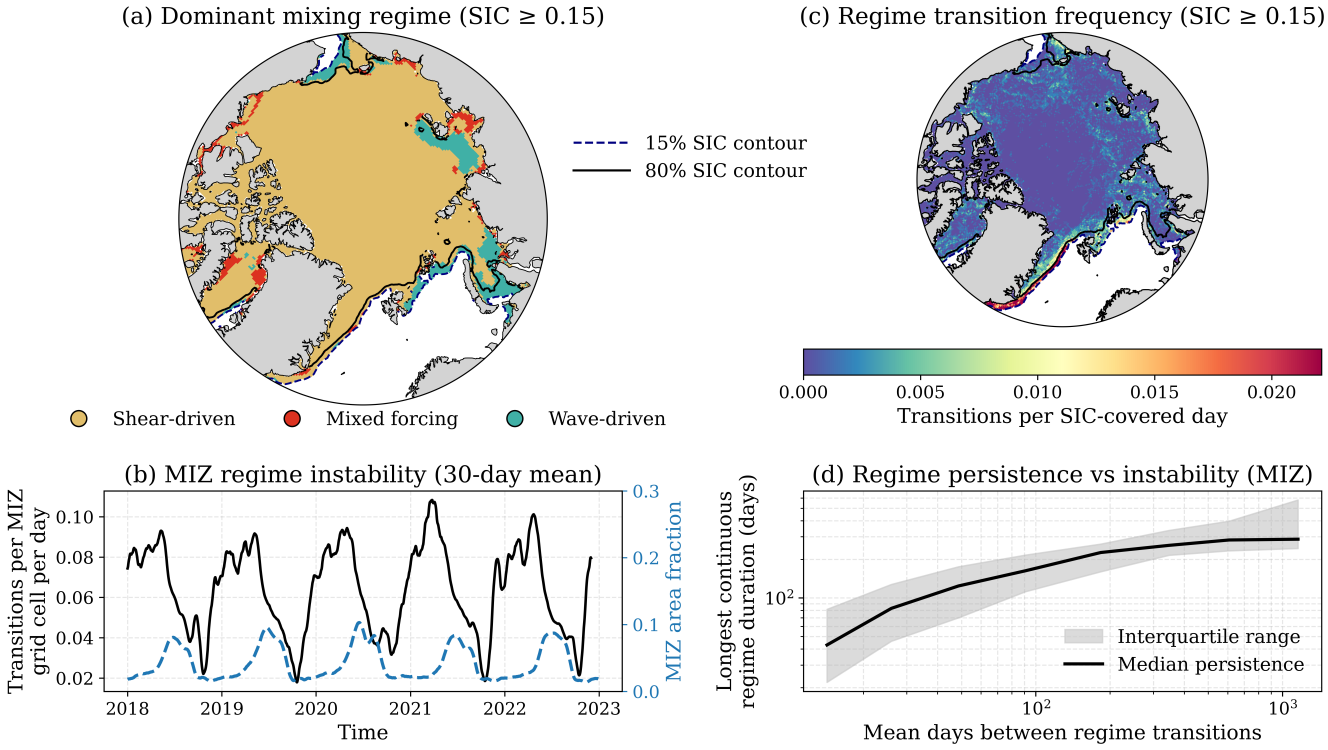

Figure 3. Spatial and temporal characteristics of upper-ocean mixing regime dynamics under sea ice for SIC ≥ 0.15. (a) Dominant mixing regime defined as the regime occupying at least 50% of SIC-covered days at each grid cell over the analysis period. Shear-driven conditions dominate the compact ice interior, while mixed and wave-driven regimes preferentially occur near the ice edge and in seasonally ice-covered regions. Dashed and solid contours indicate the 15% and 80% sea ice concentration (SIC) thresholds, respectively. (b) Normalized regime transition frequency (transitions per SIC-covered day) for SIC ≥ 0.15, highlighting enhanced temporal variability along the MIZ and reduced variability within the compact ice interior. (c) Time series of marginal ice zone (MIZ; 0.15 ≤ SIC ≤ 0.8) regime instability, defined as the fraction of MIZ grid cells undergoing at least one regime transition within a 30-day window (black), together with the contemporaneous fraction of the Arctic domain classified as MIZ (blue, dashed). (d) Relationship between regime persistence and instability within the MIZ, shown as the median longest continuous regime duration (black) and interquartile range (shading) binned by the mean number of days between regime transitions. Increasing transition frequency is associated with a systematic reduction in regime persistence.

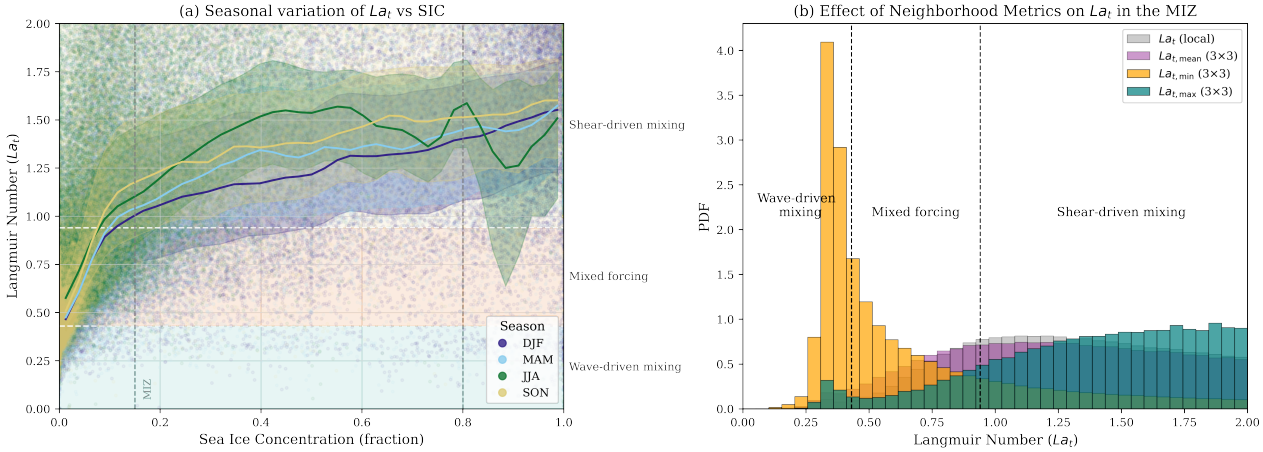

Figure 4. Sea ice concentration dependence of the turbulent Langmuir number. (**Left**) Parametric plot of La_t against binned sea ice concentration (SIC). Solid lines denote the median La_t for each season and bin, with shading indicating inter-quartile ranges. The white dashed lines mark the wave-dominated ($La_t < 0.43$) and shear-dominated ($La_t > 0.94$) regime thresholds. (**Right**) Normalized histogram of La_t values in each smoothing category, aggregated over all ice-covered grid cells (SIC ≥ 0.15). This histogram highlights the asymmetry and variability in the spatial scale and intensity of Langmuir turbulence across the Arctic.

~~Spatial and regime-dependent structure of upper ocean turbulent dissipation across the Arctic. (a) Mean dissipation rate (ε) over the 2018–2022 period, with 80% sea ice concentration (SIC) contour shown in black. (b) Relative contribution of LT to total OSBL dissipation ($\varepsilon_{\mathrm{LT}}/\varepsilon_{\mathrm{shear}}$) as a function of La_t, colored by mean SIC. Dashed lines denote La_t regime thresholds for wave-driven, mixed and shear driven mixing. The red dashed line shows the theoretical scaling $\varepsilon_{\mathrm{LT}}/\varepsilon_{\mathrm{shear}} \propto 1/La_t^2$, derived from idealized mixed-layer turbulence theory (Grant and Belcher, 2009). (c) Seasonal histogram of domain-averaged dissipation for March and September, indicating an annual modulation linked to sea ice retreat and increased wave exposure. (d) Mean dissipation enhancement due to Langmuir turbulence, quantified as $\varepsilon/\varepsilon_{\mathrm{shear}} - 1$, across sea ice regimes, illustrating the increasing energetic importance of LT in low-SIC conditions. (e) Mean fractional contribution of Langmuir-driven dissipation across SIC regimes, time-weighted over all valid time steps, emphasizing the growing role of LT in OW regions relative to compact ice.~~

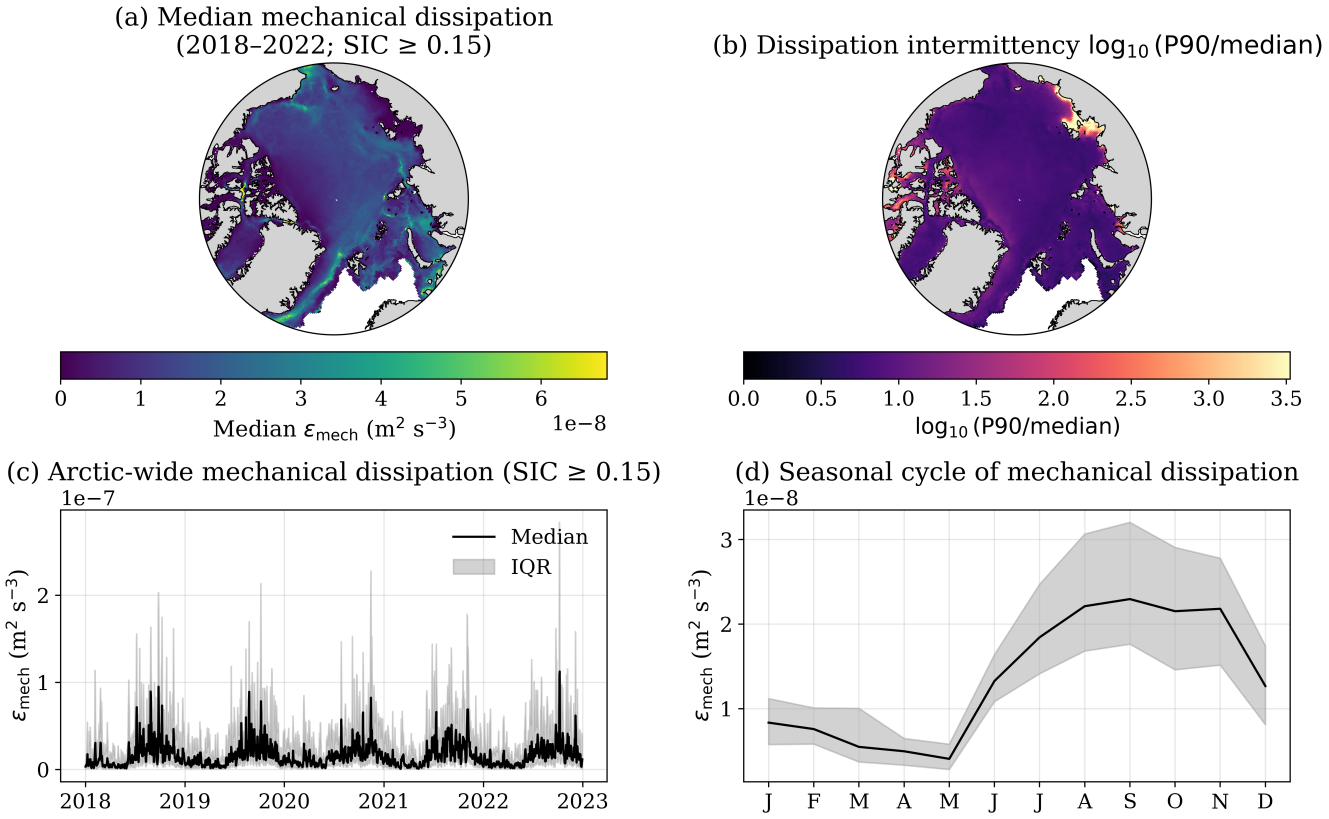

Figure 5. Mechanical dissipation magnitude and intermittency within the Arctic marginal ice zone (2018–2022). **(a)** Spatial distribution of the aggregated median mechanically forced dissipation, $\varepsilon_{\mathrm{mech}}$, evaluated for ice-covered conditions (SIC $\geq$ 0.15). **(b)** Dissipation intermittency index, defined as $\log_{10}(\mathrm{P90/median})$ of $\varepsilon_{\mathrm{mech}}$. **(c)** Arctic-wide temporal evolution of mechanically forced dissipation aggregated over all grid cells classified as MIZ (SIC $\geq$ 0.15), shown as the spatial median (black line) with interquartile range (shading), illustrating the strongly intermittent nature of MIZ energy input. **(d)** Seasonal cycle of mechanically forced dissipation within the MIZ, constructed from the monthly climatology of the spatial median in panel (c), with shading indicating the interquartile range.

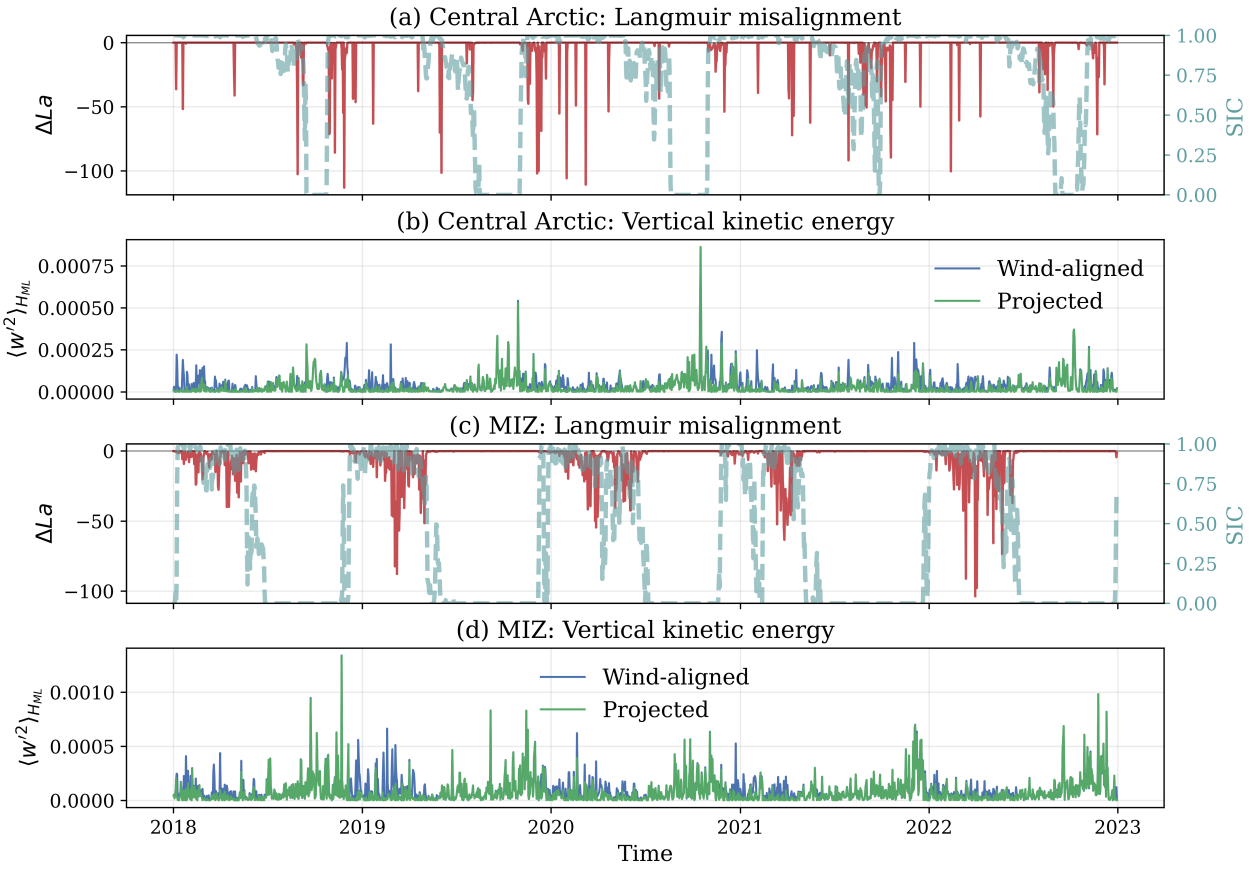

Figure 6. **Impact of wind–wave misalignment on Langmuir turbulence at representative Arctic sites.** Time series extracted at a consolidated central Arctic location (**a,b**) and a seasonal MIZ location (**c,d**). Panels **(a)** and **(c)** show the Langmuir misalignment metric $\Delta La = La_{\mathrm{proj}} - La_t$, where La_t is the wind-aligned turbulent Langmuir number and La_{proj} accounts for dynamically projected Langmuir cell orientation. Negative values indicate geometric suppression of Langmuir forcing due to wind–wave misalignment. Sea ice concentration (SIC) is overlaid on a secondary axis (dashed teal line). Panels **(b)** and **(d)** show the mixed-layer-averaged vertical velocity variance $\langle w'^2 \rangle_{H_{\mathrm{ML}}}$ estimated from LES-based scalings, comparing wind-aligned (blue) and projected (green) Langmuir forcing.

~~Together, the 2022~~

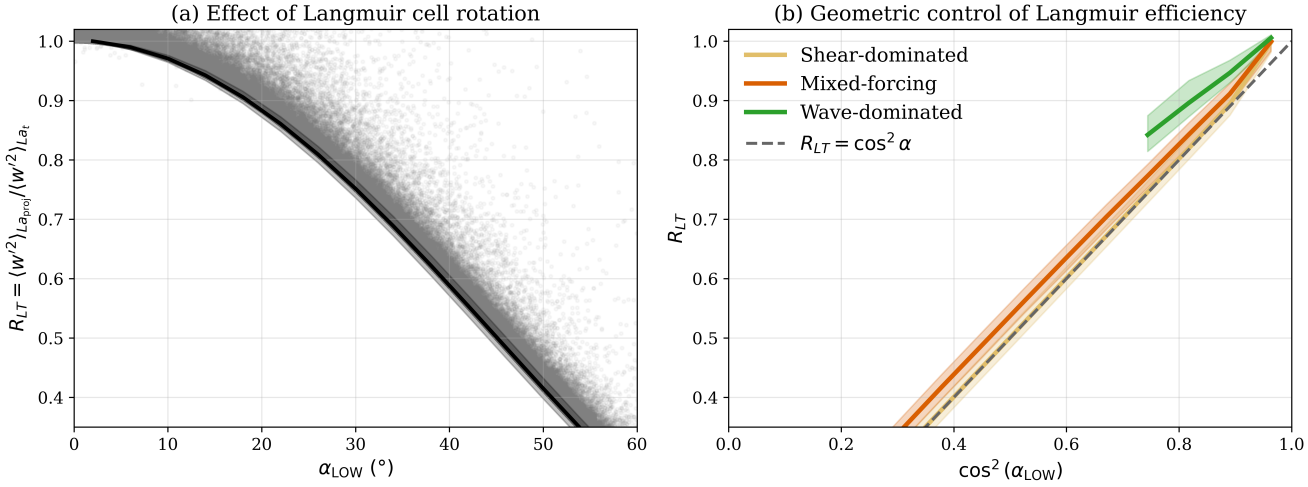

Figure 7. ~~**Langmuir turbulence diagnostics for kernel regions**~~ **Geometric control of Langmuir turbulence efficiency by wind–wave misalignment.** (~~Central Arctic and Barents Sea~~**a**) Dependence of the Langmuir efficiency factor $R_{LT} = \langle w'^2 \rangle_{La_{proj}} / \langle w'^2 \rangle_{La_t}$ on the Langmuir cell orientation angle α_{LOW} for all ice-covered grid cells. Gray points show individual grid–time samples, ~~each defined as a 5×5 gridcell~~ while the black curve and shading denote the binned median and interquartile range. (~~~100 km radius~~**b**) ~~area. **Left**: Map~~ Same data recast as a function of ~~kernel locations. **Right**: For each region~~$\cos^2(\alpha_{LOW})$, ~~time series of~~ highlighting the underlying geometric control on Langmuir ~~turbulence dissipation (ϵ_{LT})~~efficiency. Colored curves show regime-conditioned medians for shear-dominated, ~~normalised vertical kinetic energy (VKE)~~mixed-forcing, and ~~SIC for a year (2022)~~wave-dominated regimes, with shaded envelopes indicating interquartile ranges. The dashed line denotes the ideal geometric scaling $R_{LT} = \cos^2 \alpha$.

2.6 ~~Impact of Wind–Wave Misalignment on Langmuir Turbulence-Induced Dissipation in the Arctic~~

~~In this section, we compute the dissipation ratio $\varepsilon_{La_{proj}} / \varepsilon_{La_t}$ to assess how directional misalignment between wind and waves modulates~~